



FEDERAL UNIVERSITY OF PARÁ
INSTITUTE OF GEOSCIENCES
GEOPHYSICS GRADUATE PROGRAM

MASTER DISSERTATION

**Analysis of the Eshelby-Cheng model adapted for
cracked rocks with anisotropic porous backgrounds**

MURILLO JOSÉ DE SOUSA NASCIMENTO

Belém-PA
2019

MURILLO JOSÉ DE SOUSA NASCIMENTO

Analysis of the Eshelby-Cheng model adapted for cracked rocks with anisotropic porous backgrounds

Master Dissertation submitted to the Geophysics Graduate Program of the Geosciences Institute at Federal University of Pará for the obtainment of the title of Master of Science in Geophysics.

Area of study: Petrophysics

Research field: Geophysics applied to hydrocarbon exploration

Advisor: Prof. Dr. José Jadsom Sampaio de Figueiredo

Belém-PA

2019

**Dados Internacionais de Catalogação na Publicação (CIP) de acordo com ISBD
Sistema de Bibliotecas da Universidade Federal do Pará**

N244a Nascimento, Murillo José de Sousa.

Analysis of the Eshelby-Cheng model adapted for cracked rocks with anisotropic porous back-
grounds / Murillo José de Sousa Nascimento. – 2019.

54 f. : il. color.

Orientador: Prof. Dr. José Jadsom Sampaio de Figueiredo

Dissertação (Mestrado) - Programa de Pós-Graduação em Geofísica, Instituto de Geociências,
Universidade Federal do Pará, Belém, 2019.

1. Geofísica. 2. Modelagem (Geofísica). 3. Ondas sísmicas - Velocidade. I. Título.

CDD 550

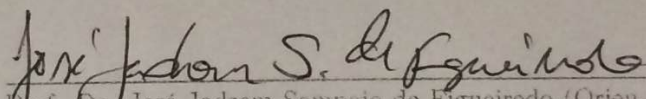
MURILLO JOSÉ DE SOUSA NASCIMENTO

Analysis of the Eshelby-Cheng model adapted for cracked rocks
with anisotropic porous backgrounds

Dissertação apresentada ao Programa de Pós-Graduação
em Geofísica da Universidade Federal do Pará para obtenção
do título de Mestre em Geofísica.

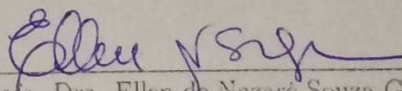
Data de aprovação: February 28, 2019

Banca Examinadora:



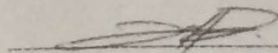
Prof. Dr. José Jadsom Sampaio de Figueiredo (Orientador)

Universidade Federal do Pará



Prof. Dra. Ellen de Nazaré Souza Gomes

Universidade Federal do Pará



Dr. Jorge Henrique Faccipieri Junior

Universidade Estadual de Campinas

ACKNOWLEDGMENTS

I would like to thank all the support given to me in terms of time, space and structure by Universidade Federal do Pará (UFPA) and Curso de Pós-Graduação (CPGF), as well as to thank all the support given to me by my Professors, mainly to my advisor Professor José Jadsom Sampaio de Figueiredo.

I am also grateful to CNPQ for the financial support during this work.

RESUMO

O conhecimento sobre as propriedades físicas das fissuras -ou fraturas- presentes nas rochas é importante para a indústria no processo de exploração de hidrocarbonetos. Várias teorias de meio efetivo são construídas para descrever as propriedades macroscópicas de um meio (da rocha, ou reservatório neste caso) em termos das propriedades de seus constituintes (a matrix e as inclusões da rocha, neste cenário). Uma teoria de meio efetivo muito conhecida é o modelo de Eshelby-Cheng, que é o modelo estudado e analisado neste trabalho. A análise é feita testando velocidades elásticas e parâmetros de Thomsen -como função da densidade de fissuras para valores fixos de razão de aspecto e como função da razão de aspecto para valores fixos de densidade de fissuras- preditos pelo modelo contra dados adquiridos de amostras de rocha sintética. Neste trabalho, nós visamos estudar as capacidades do modelo de Eshelby-Cheng quando aplicado em rochas fissuradas com matrizes porosas e anisotrópicas (verticalmente isotrópicas com eixo de simetria vertical: Vertical Transversely Isotropic - VTI), testando algumas modificações propostas às equações com o objetivo de ajustar o modelo para esse tipo de meio. Os dados usados para testar o modelo foram obtidos de 17 amostras de rocha sintética, sendo uma sem fissuras e 16 fissuradas, dado que as fissuradas são divididas em quatro grupos com quatro amostras cada, com cada grupo possuindo rochas fissuradas de forma que as fissuras possuem a mesma razão de aspecto, porém densidades de fissuras diferentes, para rochas dentro do mesmo grupo. Nestas amostras, medidas de transmissão de pulso ultrassônico foram realizadas para se obter as velocidades experimentais usadas para testar o modelo teórico. Como não foi possível adquirir dados de velocidades como função da razão de aspecto para valores fixos de densidade de fissuras, nós realizamos interpolações dos dados experimentais para estimar estes valores. As velocidades efetivas e os parâmetros de Thomsen, estimados com o modelo de Eshelby-Cheng, foram calculados usando três formulações propostas para a porosidade de fissuras: uma proposta por Thomsen, a segunda (que depende somente da densidade de fissuras) e a terceira (que depende tanto da densidade de fissuras quanto da razão de aspecto, assim como a proposta por Thomsen) são propostas neste trabalho. As comparações feitas entre velocidades elásticas e parâmetros de Thomsen preditos pelo modelo e estimados dos dados experimentais via interpolação mostram que a terceira formulação produz melhores ajustes (menores valores de erro médio quadrático) entre o modelo e o dado experimental para todas as faixas de razão de aspecto e densidade de fissuras.

Palavras-chave: Geofísica. Modelagem (Geofísica). Ondas sísmicas - Velocidade.

ABSTRACT

The knowledge about rock cracks - or fractures - physical properties is important for the industry in the process of hydrocarbon exploration. Various effective medium theories are constructed in order to describe the macroscopic properties of a medium (the rock, or reservoir in this case) in terms of the properties of its constituents (the background matrix of the rock and the inclusions, for our scenario). A very well known effective medium theory is the Eshelby-Cheng model, which is the one we analyze in this work. The analysis is done testing elastic velocities and thomsen parameters - as function of crack density for fixed values of aspect ratio and as function of crack aspect ratio for fixed values of crack density - predicted by the model against data acquired from synthetic rock samples. In this work we aim to study the Eshelby-Cheng model capabilities when applied to rocks with porous and vertical transversely isotropic (VTI) backgrounds, testing some modifications proposed to the equations in order to fine tune the model for this kind of medium. The data used to test the model were obtained from 17 synthetic rock samples, one uncracked and 16 cracked, the latter divided in four groups of four samples each, each group with cracks having the same aspect ratio, but with the samples having different crack densities. In these samples, ultrasonic pulse transmission measurements were performed in order to obtain the experimental velocities used to test the model. As was not possible to acquire data for velocity as function of aspect ratio for fixed values of crack density, we performed interpolations of the experimental data to estimate these velocities. Eshelby-Cheng model effective velocities and Thomsen parameters were calculated using three formulations proposed for the crack porosity: one proposed by Thomsen, the second one (which depends only on the crack density) and the third one (which depends on the crack porosity and the aspect ratio, just like Thomsen's proposal) are proposed in this work. The comparisons between elastic velocities and Thomsen parameters - as function of crack aspect ratio, for fixed values of crack density - predicted by the model and estimated from the data via interpolation showed that the third formulation produced better fittings (lower root-mean-square errors) between model and experimental data for all ranges of aspect ratio and crack density.

Keywords: Geophysics. Modeling (Geophysics). Seismic waves - Velocity.

LIST OF FIGURES

2.1	Workflow used to calculate the effective theoretical velocities and Thomsen parameters. Block (1) shows the input parameters, obtained from elastic parameters (V_P , V_S and ρ) measured in the background reference sample as well as the physical parameters of inclusions (α , ϵ , ϕ_{ref} and ϕ_c). Block (2) shows the output obtained from equation 2.2, i.e., the effective elastic stiffness parameters. These coefficients can be used to evaluate the Thomsen parameters, as represented by block (3), or combined with the theoretical effective density, they can be inverted on theoretical elastic velocities, as represented by block (4).	5
2.2	The black crosses show the experimental bulk density as a function of the crack density for the 16 cracked samples. To estimate the theoretical density we used equation 2.8. The red, green, blue and magenta solid lines show the theoretical densities computed by equation 2.8 with the total effective porosity ϕ_{total}^{eff} obtained using equation 2.5. The black line shows the theoretical densities computed by equation 2.8 with the porosity obtained using equation 2.7. The best fit between the estimated and experimental densities occurred for the theoretical porosity estimated by equation 2.7. Using the Thomsen (33)'s porosity equation, only in case of $\alpha = 0.2$, a reasonable fit between theory and experiments can be observed.	7
3.1	(a) Sample construction of a group of samples with inclusion's aspect ratio equal to 0.08. (b) Cylindrical samples (plugs) are obtained by a plugging machine. c) Photograph of all samples used in this work. The samples are divided by the aspect ratio of their inclusions, forming four groups ($\alpha_1 = 0.08$, $\alpha_2 = 0.2$, $\alpha_3 = 0.32$, $\alpha_4 = 0.52$) of four samples each, plus a reference -with no inclusions- sample identified as REF in the image. The experimental crack density (ϵ), aspect ratio (α) as well as the dry sample density- ρ_b and porosity (ϕ) are shown in the Table 3.1.	10

3.2	(a) Picture of the ultrasonic system setup used in this work. (b) Experimental arrangement of the transducers, in the samples, for P- and S- wave acquisitions. $S1$ and $S2$ indicate the faster and slower S-wave polarizations, respectively. P_Z indicates P-wave propagation in the Z direction. c) Experimental sketch of wave propagation direction and polarization to obtain the P- and S-waveform records. The angle θ is the angle between the direction of propagation of the P-wave and the Z axis, while φ is the angle between the direction of propagation of the S-wave and the Z axis. For the P-wave, the propagation is radial changing from $\theta = 0^\circ$ (Z direction) to $\theta = 90^\circ$ (X direction) and for S-wave, the propagation is in the Y direction and the slow and fast polarizations correspond to $\varphi = 0^\circ$ (X direction) and $\varphi = 90^\circ$ (Z direction), respectively.	12
4.1	P-wave velocities (V_{P0° , V_{P45° and V_{P90°) as function of crack density for different aspect ratios ($\alpha = 0.08, 0.2, 0.32, 0.52$) assuming dry condition. The red circles show the experimental P-wave velocities. The blue and green curves show the P-wave velocities estimated by Eshelby-Cheng model with the crack porosity calculated via equations 2.5 and 2.6, respectively.	14
4.2	S-wave velocities (V_{SH} and V_{SV}) as function of crack density for different aspect ratios ($\alpha = 0.08, 0.2, 0.32, 0.52$) assuming dry condition. The red circles show the experimental S-wave velocities. The blue and green curves show the S-wave velocities estimated by Eshelby-Cheng's model with the crack porosity calculated via equations 2.5 and 2.6, respectively.	16
4.3	The red circles show the experimental crack sample porosities as function of the crack density for the sixteen cracked samples. To estimate the theoretical crack densities we used equations 2.5 and 2.6. The best fit between the estimated and experimental density occurred for theoretical porosity estimated by equation 2.7. Using the Thomsen (33)'s porosity equation, only in case of $\alpha = 0.2$, a reasonable fitting between theory and experiments can be observed.	17
4.4	Thomsen Parameters (γ , ε and δ) as function of crack density for different aspect ratios: $\alpha = 0.08, 0.2, 0.32, 0.52$. The red circles show the Thomsen Parameters obtained from the experimental velocities. The blue and green curves show the Thomsen Parameters obtained from the velocities estimated by Eshelby-Cheng's model with crack porosity calculated using equations 2.5 and 2.6, respectively.	18

4.5	Interpolation performed to the velocities as function of crack density in order to produce an estimative of velocities as function of crack aspect ratio. Each column is associated with a fixed value of crack aspect ratio, while each graph shows velocities as function of crack density. The blue circles represent the experimental velocity data. The red lines represent the linear interpolation of the experimental data.	19
4.6	Linear regression performed to the Thomsen parameters as function of crack density in order to produce an estimative of Thomsen parameters as function of crack aspect ratio. Each column is associated with a fixed value of crack aspect ratio, while each line of graphs shows a Thomsen parameter as function of crack density. The blue circles represent the Thomsen parameters calculated directly from experimental data. The red lines represent the linear interpolation of the data.	20
4.7	The vertical axis shows values of velocity, while the horizontal axis shows values of crack aspect ratio. Each line of graphs shows an elastic velocity with a specific direction of propagation, while each column of graphs is related to a fixed value of crack density. The purple circles represent the velocity values obtained via interpolation of the experimental data. All three curves represent velocity values calculated using the Eshelby-Cheng model workflow shown in Figure 2.1, but the blue continuous curves represent the velocity values calculated using the crack porosity estimated by equation 2.5, while the red dashed curves represent the velocity values calculated using the crack porosity estimated by equation 2.6 and the yellow curves made of dashes and points represent the velocities calculated using the model fed by crack porosity equation 2.9.	22

4.8	The vertical axis shows values of the Thomsen parameters -which are dimensionless and vary always between zero and one- while the horizontal axis shows values of crack aspect ratio. The first line of graphs shows the values for the ϵ parameter (also known as P-wave anisotropy), the second line of graphs shows the values for the γ parameter (also known as P-wave anisotropy) and the third line shows the values for the δ parameter, which is related both to P- and S-waves, while each column is associated to a fixed value of crack density. The purple circles represent the parameters values obtained via interpolation of the experimental data. All three curves represent parameters obtained from velocities calculated using the Eshelby-Cheng model workflow shown in Figure 2.1, but the blue continuous curves represent the velocity values calculated using the crack porosity estimated by equation 2.5, while the red dashed curves represent the velocity values calculated using the crack porosity estimated by equation 2.6 and the yellow curves made of dashes and points represent the velocities calculated using the model fed by crack porosity equation 2.9.	23
5.1	Velocity maps produced using Eshelby-Cheng effective medium theory. The colors represent the velocity values in m/s . the vertical axis shows values of crack density, while the horizontal axis shows values of aspect ratio. Each line of maps shows one of the five elastic velocities studied in this work. Each column of maps is associated with one of the three crack porosity equations tested in this work. There are some regions in the maps (first line, second column and fourth line, second column) in which the model, using 2.6, produced complex valued velocities, that is, unphysical results.	29
5.2	Root-mean-squared error between elastic velocities calculated from the Eshelby-Cheng model, using the three crack porosity formulations, and experimental elastic velocities. The errors are shown for each fixed crack density associated to the graph from which the velocity errors were calculated. (a) P-wave velocity errors. (b) S-wave velocity errors.	30
5.3	Root-mean-squared error between Thomsen parameters calculated from the Eshelby-Cheng model, using the three crack porosity formulations, and experimental elastic velocities. The errors are shown for each fixed crack density associated to the graph from which the anisotropic parameter errors were calculated.	31
7.1	(a) P- and (b) S-waveforms for reference sample in dry condition.	35
7.2	P-wave seismograms for samples with aspect ratio $\alpha_1 = 0.08$ in dry condition.	35
7.3	S-wave seismograms for samples with aspect ratio $\alpha_1 = 0.08$ in dry condition.	36

CONTENTS

1	INTRODUCTION	1
2	THEORETICAL BACKGROUND	3
3	METHODOLOGY	8
3.1	EXPERIMENTAL SETUP	8
3.1.1	Sample Preparation	8
3.1.2	Ultrasonic measurements	11
4	RESULTS	13
4.1	ANALYSIS OF MODEL AS A FUCTION OF CRACK DENSITY	13
4.1.1	Elastic velocities	13
4.1.2	Thomsen Parameters	15
4.2	ANALYSIS OF MODEL AS A FUCTION OF CRACK ASPECT RATIO	17
4.2.1	Data interpolation	17
4.2.2	Elastic velocities	20
4.2.3	Thomsen parameters	21
5	DISCUSSIONS	25
6	CONCLUSIONS	32
7	APPENDIX	34
7.1	APPENDIX A- P- AND S-WAVEFORMS	34
7.2	APPENDIX B- ESHELBY-CHENG EFFECTIVE MODEL	34
7.3	APPENDIX C-EFFECTIVE THOMSEN PARAMETER	38
	Bibliography	40

1 INTRODUCTION

The Earth's Crust has a complex distribution of geological features as, for example: fractures, cracks, faults, folds, etc (7; 10). Over the years, the analysis of crack physical characteristics (length, aperture, orientation, and aspect ratio) and their related properties (e.g., porosity, density, and intensity) as well as their influence on seismic waves propagation have attracted considerable interest in the academy and industry. This occurs because, in certain reservoirs, called non-conventional, hydrocarbon production is dependent on induced permeability caused by hydraulic fracturing in the cracked medium (31; 35). The knowledge about crack features, mentioned earlier, is an important stage in the process of hydrocarbon recovering, e. g., the presence of oriented cracks may induce an anisotropic behavior in a medium (11; 25). Regions with oriented cracks have their seismic wave velocities varying with both propagation and polarization directions (13; 29; 35). Thus, the analyses of the behavior of seismic wave velocities in a cracked medium can be used as a tool for reservoir characterization (17).

Effective elastic properties, V_P and V_S , of anisotropic rocks can be estimated by theoretical and experimental approaches. From a theoretical point of view, we can highlight effective models created for: transversely cracked medium with low crack density (16; 22) and high crack density (9; 23; 20) to investigate the effect of scale fracture length, equant porosity (33; 8) and the host medium's weak anisotropy (19). Experimentally, many of effective medium theories cited previously have been investigated by several works. Assa'd et al. (2, 3); Boadu and Long (6), Rathore et al. (27) and Ding et al. (15) investigated the Hudson (22)'s effective medium theory for low crack density medium through remarkable experiments. Tillotson et al. (34) and Amalokwu et al. (1) using synthetic crack porous sandstones, constructed from the improved technique developed by Rathore et al. (27), investigated the effective Chapman (8)'s model applied into frequency-dependent seismic anisotropy in synthetic fractured reservoir. More recently, Henriques et al. (21) compared predictions of effective elastic parameters -in anisotropic cracked media- by (22) and Eshelby-Cheng's effective models with experiments performed in cracked samples showing different aspect ratios in their composition. They observed that, in general, the Eshelby-Cheng's effective model showed a good agreement with the experimental results.

Even though many works have been performed in order to investigate the feasibility of applying effective models into ultrasonic (2; 27; 1; 21), well-sonic (37) and seismic (5; 4) datasets, a better understanding of limitations and applicability of these effective models is still required, especially in the case where the background presents a certain degree of anisotropy. In this work, we investigate the application of Eshelby-Cheng's effective model for porous cracked samples with different crack aspect ratios, 0.08 to 0.52, and different crack densities, 0.01 to 0.102, considering the background with a weak VTI

anisotropy. For this study, we constructed sixteen synthetic porous cracked samples and one uncracked sample for reference. The cracks were simulated physically with void spaces created by chemical leaching of styrofoam penny-shaped inclusions. Compressional and shear wave velocities as well as anisotropic parameters were estimated experimentally and compared with the results obtained via effective Eshelby-Cheng's cracked model. From both the theoretical and experimental results we observed a decreasing of elastic velocities and an increasing of anisotropy behavior with increasing of crack density, for all groups of aspect-ratio samples. From the comparisons between theoretical and experimental results we observed that the performance of Eshelby Cheng's model in predicting the anisotropic velocities and parameters, in a cracked medium, for different crack's aspect ratios depends on the porosity equation chosen to feed the effective model.

Due to technical difficulties in the experiment, it was not possible to construct samples with different aspect ratios but same crack densities, therefore it was not possible to acquire the data necessary to obtain the experimental velocities as function of aspect ratio. In this work we aim to fill this gap, by estimating velocities as function aspect ratio - for fixed crack densities - via interpolation of the original data, and then to perform the comparisons between data and model predictions (again testing the alternatives for the model porosity) in order to complete the previously-mentioned investigation of the model. Furthermore, as the velocities predicted by the model fed with a crack porosity dependent only on crack density (and not on crack aspect ratio) showed some mathematical inconsistencies in certain regions of the parameter-space constituted by crack density and crack aspect ratio (the two main variables of the problem), we propose in this work a third formulation for the crack porosity, adapted from Thomsen's formulation and from our previous formulation, which is dependent on both cracks aspect ratio and density and tries to incorporate to the crack porosity the fact that the background is porous.

2 THEORETICAL BACKGROUND

Based on an expansion of Padé approximation, Cheng (9) improved the mathematical formulations of Eshelby (16) and Hudson (22) effective models. With this expansion, Cheng (9) solved the problem of divergence at high crack densities. Mathematically, the Eshelby-Cheng's model is given by

$$C_{ij}^{eff} = C_{ij}^{(0)} - \phi C_{ij}^{(1)}, \quad (2.1)$$

where $C_{ij}^{(0)}$ is the isotropic elastic coefficient, associated to the host material, ϕ is the medium porosity and $C_{ij}^{(1)}$ is the first order correction due to crack inclusions. In this model, the input parameters used to feed the model are: rock sample density (ρ_{total}^{iso}), isotropic P-wave velocity (V_P^{iso}), isotropic S-wave velocity (V_S^{iso}), crack density (ϵ), and crack aspect ratio (α).

As mentioned above, our background medium shows a weak VTI anisotropy due to the layering deposition. In this way, we propose to modify the equation 2.1 to

$$C_{ij}^{eff(dry,sat)-mod} = C_{ij}^{(0)-VTI(dry,sat)} - \phi^{eff(dry,sat)} C_{ij}^{(1)-mod}, \quad (2.2)$$

where $C_{ij}^{(0)-VTI(dry,sat)}$ is the elastic coefficient for the VTI background medium. The $C_{ij}^{(1)-mod}$ and ϕ^{eff} are the first order correction of the modified elastic moduli and the medium porosity, respectively.

An important issue raised in this work relies on the conversion of effective elastic parameters, output from Eshelby-Cheng's model- $C_{ij}^{eff(dry,sat)-mod}$, into effective elastic velocities. Figure 2.1 shows a flowchart to use Eshelby-Cheng's model. It is important to mention that this flowchart can be used for other stiffness coefficient models based on information of background and inclusions. The first block of this flowchart is related to the input information of the host, or background, medium obtained from elastic parameters $-V_P, V_S$ and ρ - as well as the physical parameters of inclusions $-\alpha, \epsilon, \phi_{ref}$, and ϕ_c -. The second block is feed by information of block (1). It provides the output obtained from equation 2.2, i.e., the effective elastic stiffness coefficients. These coefficients can be used to estimate the Thomsen parameters, as represented by block (3), or combined with the theoretical effective density, they can be inverted on theoretical elastic velocities, as represented by block (4).

Here, block (4) of Figure 2.1 shows the influence of theoretical effective sample density to obtain the effective velocities. As shown in block (2), also in Figure 2.1, the effective theoretical density for dry condition depends on the effective sample porosity. The total

effective porosity can be estimated by

$$\phi_{total}^{eff(exp)} = \phi_{matrix}^{ref(exp)} + \phi_c^{eff}, \quad (2.3)$$

where $\phi_{matrix}^{ref(exp)}$ is the porosity of uncracked sample estimated experimentally and ϕ_c^{eff} is the crack porosity. Experimentally, the crack porosity (ϕ_c^{eff}) can be estimated from

$$\phi_c^{eff} = \phi_{total}^{eff(exp)} - \phi_{matrix}^{ref(exp)}, \quad (2.4)$$

where "(exp)" means the measured porosity by a porosimeter.

By definition of effective model, we can not use the equation 2.4 to find the ϕ_c^{eff} . Because, the effective model is feed only from ϵ , α , density and velocities of the reference sample. On the other hand, one possible approach is the one done by Thomsen (33), who estimates the crack porosity by

$$\phi_c = \phi_c^{Thom} = \frac{4}{3}\pi\epsilon\alpha, \quad (2.5)$$

where ϵ is the crack density and α is the crack aspect ratio. This equation was formulated taking into account many assumptions. Among them, the medium should show weak anisotropy (low crack density), the cracks should show low crack aspect ratio and should not interact with each other, i.e., should have no regions of intersection. In our case, there is no interaction between cracks and the aspect ratio ranges from 0.08 to 0.52. In other words, most of our crack aspect ratios are higher than 0.1.

Another approach is to use the geometrical features of the cracked samples to estimate the effective crack porosity. This leads to

$$\phi_c = \epsilon(1 - \phi_{matrix}^{ref}), \quad (2.6)$$

and

$$\phi_{total}^{eff} = \phi_{matrix}^{ref} + \epsilon(1 - \phi_{matrix}^{ref}), \quad (2.7)$$

where ϕ_{matrix}^{ref} is the experimental reference sample porosity and ϵ is the crack density, for this we consider the theoretical effective crack porosity as the crack density minus the contribution of primary porosity, i. e., $\epsilon(1 - \phi_{matrix}^{ref})$.

Figure 2.2 shows experimental values, as black crosses, of sample density as function of sample crack density for all samples depicted in the Figure 3.1. The lines are the theoretical density given by

$$\rho_{total}^{eff} = \rho_{min}(1 - \phi_{total}^{eff}) + \rho_{fl}\phi_{total}^{eff}, \quad (2.8)$$

where the ϕ_{total}^{eff} can be obtained from equations 2.3 and 2.5 or, the one proposed in this

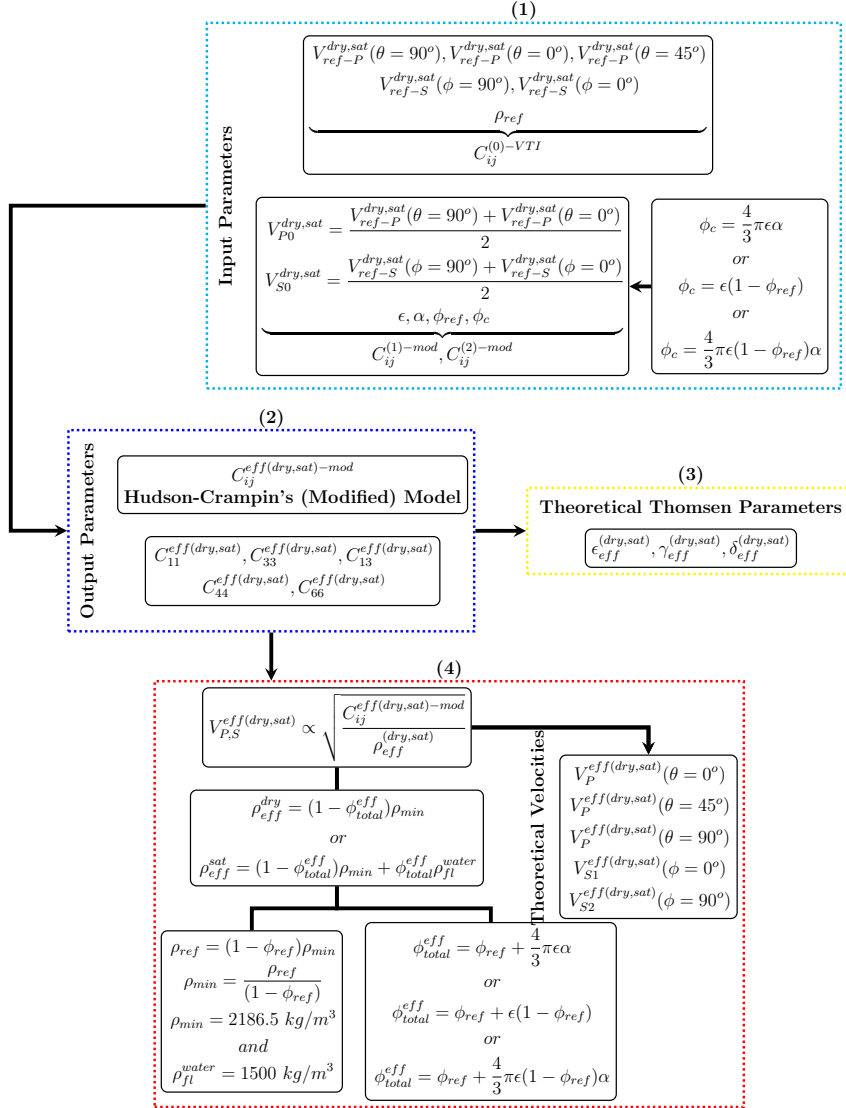


Figure 2.1: Workflow used to calculate the effective theoretical velocities and Thomsen parameters. Block (1) shows the input parameters, obtained from elastic parameters (V_P, V_S and ρ) measured in the background reference sample as well as the physical parameters of inclusions ($\alpha, \epsilon, \phi_{ref}$ and ϕ_c). Block (2) shows the output obtained from equation 2.2, i.e., the effective elastic stiffness parameters. These coefficients can be used to evaluate the Thomsen parameters, as represented by block (3), or combined with the theoretical effective density, they can be inverted on theoretical elastic velocities, as represented by block (4).

work, equation 2.7. As it can be noted, the effective density equation 2.8 that uses the equation 2.7, shown in the black curve, better predicts the effective density when compared with the experimental values for the dry condition. In case of using the Thomsen (33)'s crack porosity equation the reasonable agreement with the experimental values occurred only for $\alpha = 0.2$.

Moreover, we propose an additional formulation, which combines both of the crack porosities previously shown:

$$\phi_c = \frac{4}{3}\pi\epsilon(1 - \phi_o)\alpha, \quad (2.9)$$

which is a linear function of α and ϵ , just like the first formulation, but tries to incorporate the effect of the background porosity - to be more precise, to exclude the influence of the background porosity from the crack porosity. The applications of the adapted models are summarized in the following workflow, which also describes the measurements needed to calculate the input parameters that, in turn, are used in equation 2.2 in order to get the effective elastic stiffness coefficients.

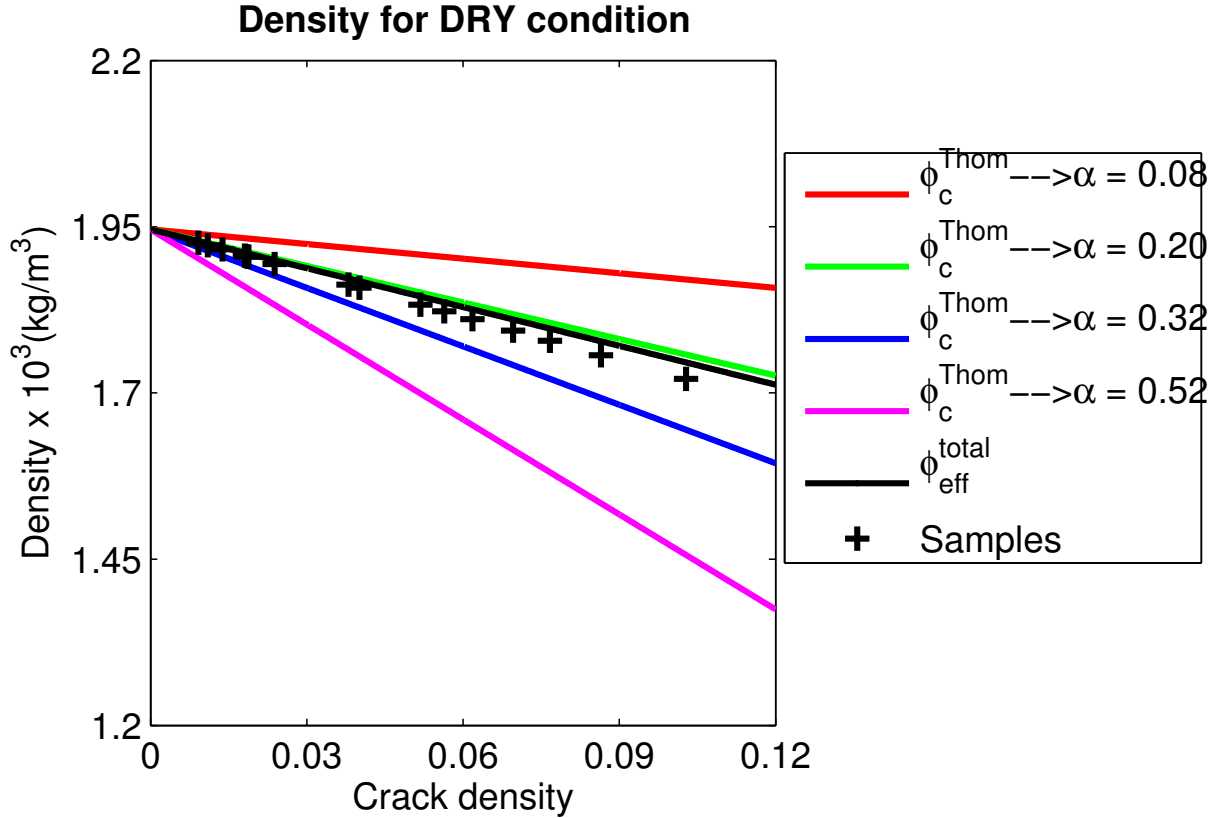


Figure 2.2: The black crosses show the experimental bulk density as a function of the crack density for the 16 cracked samples. To estimate the theoretical density we used equation 2.8. The red, green, blue and magenta solid lines show the theoretical densities computed by equation 2.8 with the total effective porosity ϕ_{total}^{eff} obtained using equation 2.5. The black line shows the theoretical densities computed by equation 2.8 with the porosity obtained using equation 2.7. The best fit between the estimated and experimental densities occurred for the theoretical porosity estimated by equation 2.7. Using the Thomsen (33)'s porosity equation, only in case of $\alpha = 0.2$, a reasonable fit between theory and experiments can be observed.

3 METHODOLOGY

3.1 EXPERIMENTAL SETUP

The construction of the synthetic rock samples as well as the ultrasonic measurements were performed at the "Dr. Om Prakash Verma" Petrophysics and Rock Physics Laboratory (PRPL) at the Federal University of Pará, Brazil.

3.1.1 Sample Preparation

The samples were constructed based on the method developed by Santos et al. (30). From a mixture of water, sand (65 %) and cement (35%), seventeen porous samples were constructed under controlled condition. On these samples, sixteen are anisotropic, VTI background with cracks, and one is purely VTI without inclusions. These sixteen anisotropic cracked samples were divided in four groups, each with four samples, with different crack aspect ratio. During the construction of the layered sample with styrofoam penny-shaped inclusions, before laying down each one of the styrofoam holder layers, a small vertical stress is applied onto the mixture (mentioned earlier) with the help of a steel buffer to ensure layer interface flatness. This process of applying pressure perpendicularly to the layer interfaces causes a preferential grain orientation -due to packing- in each of the layers, inducing small anisotropy in the background: the γ Thomsen (32) parameter is about 5 %. To create penny-shaped voids, a chemical leaching using paint thinner was performed. All samples including other test samples were immersed in paint thinner for around 24 hours. These test samples were cut in order to verify the absence of styrofoam at the cracks after leaching. As the styrofoam is a polymer made by 98 % of air and 2 % of polystyrene (26), after the leaching a practically zero amount of polystyrene mass remains inside the fracture. The sample crack density was estimated by the modified Hudson (22)'s equation given by

$$\epsilon = N_i \frac{\pi h_i r_i^2}{V_m}, \quad (3.1)$$

where N_i is the total number of penny-shaped inclusions, h_i is the aperture (thickness) of the inclusion, r_i is the radius of the inclusion and V_m is the model volume occupied only by cracks.

The aspect ratio of a form is the ratio between two different dimensions of it, for our cracks, considering its cylindrical form, the aspect ratio is

$$\alpha = \frac{h_i}{D_i},$$

where h_i and $D_i = 2r_i$ are the crack aperture and diameter, respectively.

Table 3.1: Sample parameters description (part I): D = sample diameter; H = sample height; h_i = crack aperture; N = number of inclusions. The separation between crack planes was 5 mm.

Sample	D (mm)	H (mm)	h_i (mm)	N	α	ϵ	ρ_{dry}	ρ_{sat}	ϕ
Reference	38.00	59.00	0	0	0.00	0.0000	1.9460	2.0560	0.1100
$\alpha_1\epsilon_1$	38.00	53.00	0.50	54	0.08	0.0092	1.9260	2.0451	0.1191
$\alpha_1\epsilon_2$	38.00	53.90	0.50	72	0.08	0.0138	1.9159	2.0396	0.1237
$\alpha_1\epsilon_3$	38.00	51.10	0.50	90	0.08	0.0181	1.9065	2.0346	0.1281
$\alpha_1\epsilon_4$	38.00	51.10	0.50	90	0.08	0.0238	1.8939	2.0277	0.1338
$\alpha_2\epsilon_1$	38.00	55.50	1.25	18	0.20	0.0110	1.9220	2.0430	0.1210
$\alpha_2\epsilon_2$	38.00	54.10	1.25	30	0.20	0.0188	1.9050	2.0338	0.1288
$\alpha_2\epsilon_3$	38.00	55.70	1.25	66	0.20	0.0401	1.8584	2.0085	0.1501
$\alpha_2\epsilon_4$	38.00	52.50	1.25	96	0.20	0.0618	1.8108	1.9826	0.1718
$\alpha_3\epsilon_1$	38.00	52.50	2.00	18	0.32	0.0185	1.9054	2.0340	0.1286
$\alpha_3\epsilon_2$	38.00	51.31	2.00	36	0.32	0.0380	1.8630	2.0110	0.1480
$\alpha_3\epsilon_3$	38.00	51.83	2.00	54	0.32	0.0564	1.8228	1.9891	0.1663
$\alpha_3\epsilon_4$	38.00	50.81	2.00	72	0.32	0.0767	1.7784	1.9650	0.1866
$\alpha_4\epsilon_1$	38.00	61.15	3.75	36	0.52	0.0518	1.8328	1.9946	0.1618
$\alpha_4\epsilon_2$	38.00	60.60	3.75	48	0.52	0.0696	1.7937	1.9734	0.1797
$\alpha_4\epsilon_3$	38.00	61.00	3.75	60	0.52	0.0865	1.7569	1.9534	0.1965
$\alpha_4\epsilon_4$	38.00	61.60	3.75	72	0.52	0.1028	1.7213	1.9341	0.2128

For values of aspect ratio much smaller than one, the cylindrical cracks look like discs or low aspect ratio penny shaped cracks, this is our case. For accentuated values of aspect ratio, greater than one, the cylindrical cracks are considered as needle forms. As spheres have aspect ratio equal to one, cracks that exhibit aspect ratio close to one are considered approximated by spheres.

Figure 3.1a shows the construction of four samples of group (1) which the crack aspect ratio was 0.08. In the same figure, different number of inclusions per layer means different crack densities. As it can be noted, as required by Eshelby-Cheng's model, there is no interaction among the cracks (styrofoam penny-shaped inclusions). The crack density of all samples as well as the crack aspect ratios are depicted in the Table 3.1. The sample in a cylindrical shape, as seen in Figure 3.1b, was obtained from a plugging machine from CoreLab instruments. Figure 3.1c shows a photograph of all seventeen samples investigated in this work. In each sample group, the crack density is changing according to Table 3.1. Among many parameters, the sample porosity and the sample density are shown in the Table 3.1. The samples' densities were calculated from their mass, weighted by a balance with precision of ± 0.02 g, and their volume, obtained from the samples' dimensions and the relation for the volume of a cylinder. The samples' porosities were measured by a helium porosimeter of CoreLab (reference is Ultra-pore 300).

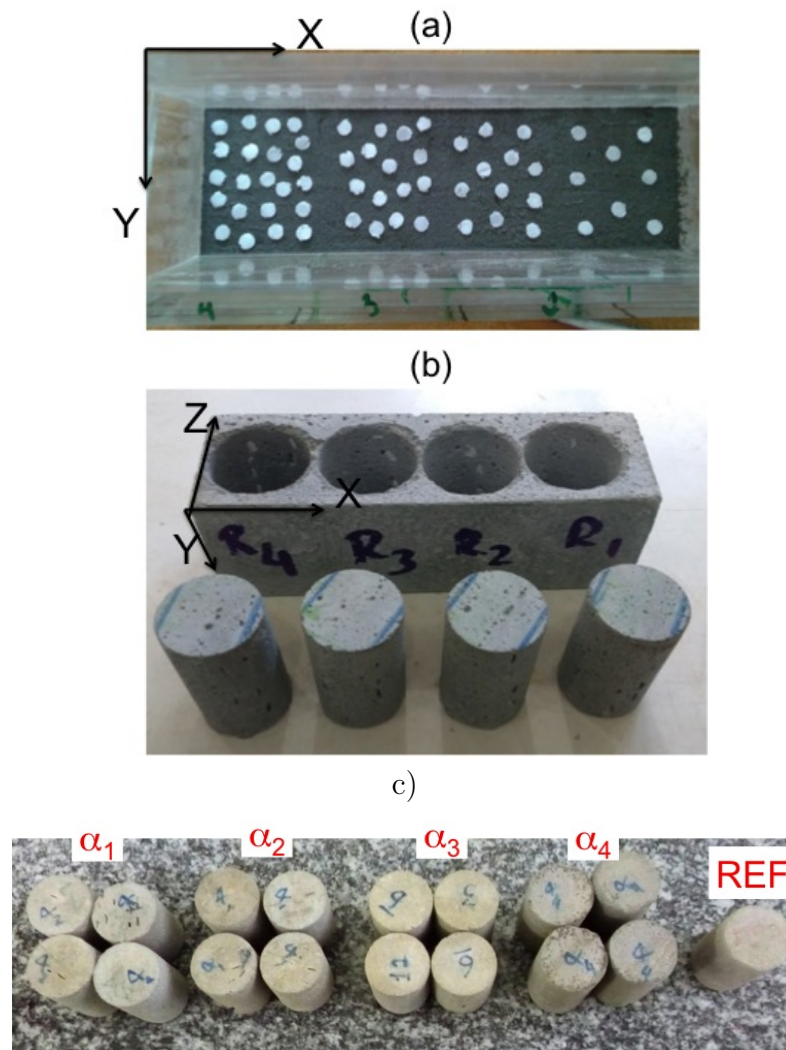


Figure 3.1: (a) Sample construction of a group of samples with inclusion's aspect ratio equal to 0.08. (b) Cylindrical samples (plugs) are obtained by a plugging machine. (c) Photograph of all samples used in this work. The samples are divided by the aspect ratio of their inclusions, forming four groups ($\alpha_1 = 0.08$, $\alpha_2 = 0.2$, $\alpha_3 = 0.32$, $\alpha_4 = 0.52$) of four samples each, plus a reference -with no inclusions- sample identified as REF in the image. The experimental crack density (ϵ), aspect ratio (α) as well as the dry sample density- ρ_b and porosity (ϕ) are shown in the Table 3.1.

3.1.2 Ultrasonic measurements

We performed the transmission measurements using a 500 kHz S-wave transducer that allows registering both P- and S-waveforms in a single trace. The sampling rate per channel for all measurements was $0.01 \mu\text{s}$. We also used a pulse-receiver 5072PR and a pre-amplifier 5660B from Olympus and a USB oscilloscope of 200 Ms/s from Hantek (reference DSO 3064). Figure 3.2a shows the picture of experimental setup used in this work. Our transducer has an intrinsic delay time of $0.14 \mu\text{s}$ (28) in its signal, which must be taken into account when estimating the wave velocities. The complete description of ultrasonic experimental setup including the frequency source spectra is described in Santos et al. (28) and in Henriques et al. (21). The source and receiver transducers were placed on opposite sides of the synthetic rocks, separated by their lengths, in this case, sample diameter or height. To ensure that the propagation of the wave was in the desired region of the samples, the transducers were placed at the center of either side. This was made for both wave modes of propagation (see Figure 3.2b).

From the first arrival pickings of the acquired P- and S-waveforms we calculated the P- and S-wave velocities. We obtained the five experimental velocities using three P-wave traces - $t_P(\theta)$ and two S-wave traces - $t_S(\varphi)$, from equations

$$V_P(\theta) = \frac{D}{t_P(\theta) - \Delta t_{delay}}, \quad (3.2)$$

and

$$V_S(\varphi) = \frac{L_Y}{t_S(\varphi) - \Delta t_{delay}}, \quad (3.3)$$

where D , L_Y and Δt_{delay} are the sample diameter (distance of P-wave propagation), the longitudinal height (distance of S-wave propagation) and the delay time due to the P and/or S-wave transducers, respectively. It is assumed that the velocities obtained via this procedure are phase velocities, due to the fact that the transducers are wide and their diameters are comparable with sample sizes (Dellinger and Vernik). As we are dealing with phase velocities, they can be easily inverted to obtain the coefficients of the stiffness tensor. For P-wave velocities, the traces recording the $\theta = 0^\circ$, 45° and 90° corresponding to the propagation along the Z axis, along the bissectrix of Z and X axes, and propagation along the X axis, respectively. The polarization of $\varphi = 0^\circ$ correspond to the fast S-wave (S1 or SH) and $\varphi = 90^\circ$ corresponds to the slow S-wave (S2 or SV). Figure 3.2c shows the sketch of the directions and polarizations of P- and S-wave propagation to record the P- and S-wave seismograms. The axes X , Y and Z are the reference axes on the samples, the XY plane corresponds to the crack planes, while the Z axis is perpendicular to them.

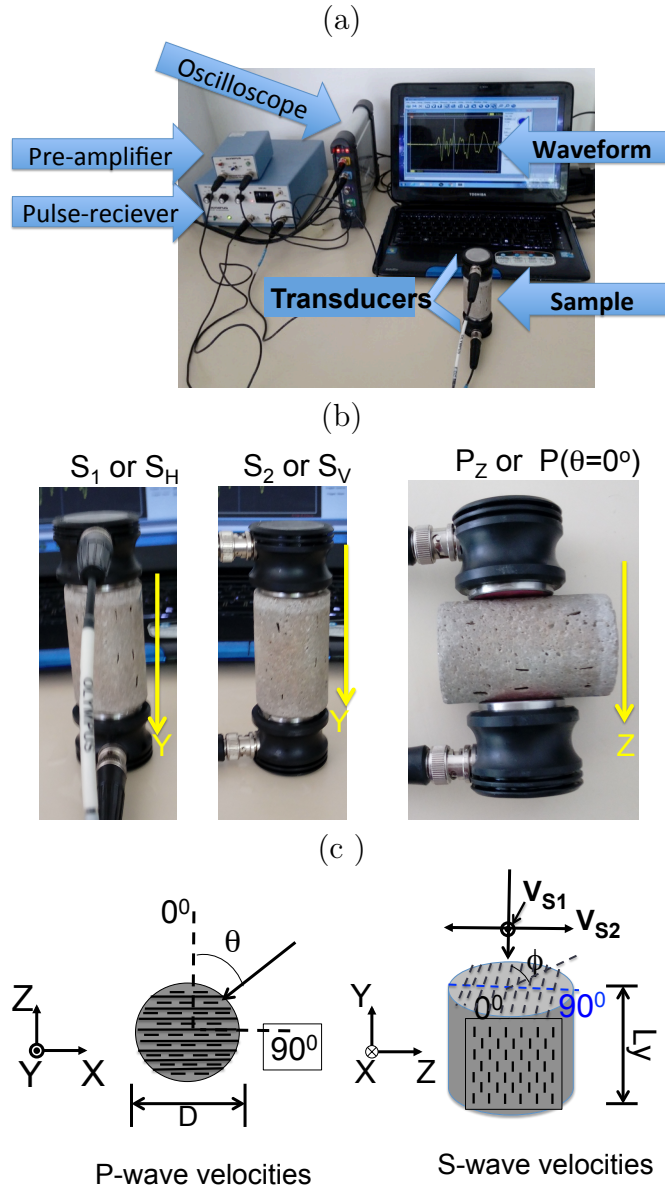


Figure 3.2: (a) Picture of the ultrasonic system setup used in this work. (b) Experimental arrangement of the transducers, in the samples, for P- and S- wave acquisitions. S_1 and S_2 indicate the faster and slower S-wave polarizations, respectively. P_z indicates P-wave propagation in the Z direction. (c) Experimental sketch of wave propagation direction and polarization to obtain the P- and S-waveform records. The angle θ is the angle between the direction of propagation of the P-wave and the Z axis, while φ is the angle between the direction of propagation of the S-wave and the Z axis. For the P-wave, the propagation is radial changing from $\theta = 0^\circ$ (Z direction) to $\theta = 90^\circ$ (X direction) and for S-wave, the propagation is in the Y direction and the slow and fast polarizations correspond to $\varphi = 0^\circ$ (X direction) and $\varphi = 90^\circ$ (Z direction), respectively.

4 RESULTS

In this chapter, we start showing the results of the ultrasonic experiments from P- and S-waves first arrival pickings. The time delays for the P- and S-wave transducers, 0.14 μs for both, were subtracted from the picked traveltimes. Using the corrected traveltimes and the distance between the transducers (sample diameter for P-wave and sample height for S-wave), wave velocities were calculated using equations 3.2 and 3.3. From these velocities, we calculated the Thomsen parameters (ϵ , γ and δ) for all samples considering the possible errors due to measurements of length, margin of error = ± 0.02 cm, and traveltime picking, margin of error = ± 0.02 μs .

4.1 ANALYSIS OF MODEL AS A FUNCTION OF CRACK DENSITY

4.1.1 Elastic velocities

From first arrival picking on P- and S-waveforms, such as shown in the Appendix A 7.1, P- and S-wave velocities were estimated. Table 4.1 shows the values of P- and S-wave velocities calculated for dry condition. From a graphical point of view, Figure 4.1 shows the three P-wave velocities, mentioned before, as function of crack density (ϵ) for different crack aspect ratios: $\alpha = 0.08, 0.20, 0.32$ and 0.52 . In general, the best fitting of Eshelby-Cheng's predictions occurs for low crack densities ($\epsilon < 10\%$), this happens for all crack aspect ratios. As it can be noted in the blue curves of Figure 4.1, there is a tendency to crack aspect-ratios 0.08 and 0.2 being better predicted for Eshelby-Cheng's model using the crack porosity equation given by $\phi_c^{Thom} = \frac{4}{3}\alpha\epsilon$. For theoretical estimation (green curve) using the crack porosity equation $\epsilon(1 - \phi_{matrix}^{ref})$, the best theoretical predictions rely on the higher aspect-ratios: 0.32 and 0.52.

With the exception of the P-wave propagation in the X-axis, the other two P-wave velocities (in the directions 45° and 90°) show a remarkable decrease with increasing of the crack density and aspect ratio. Both the theoretical and experimental values follow the same trend, however, the distance between them became significant when crack density is higher than 3 % for all crack aspect ratios. Related to the P-wave propagations, the fitting between experimental and theoretical curves is the best for $V_P(\theta = 90^\circ)$, i. e., wave propagation parallel to the crack plane (less scattering) and the worst for $V_P(\theta = 0^\circ)$, i. e., wave propagation perpendicular to the crack plane (more scattering). When fed by the porosities of equation 2.6 Eshelby-Cheng's model shows the best adjustment with experimental values.

Figure 4.2 shows the two S-wave velocities, fast and slow, as function of crack density (ϵ) for different crack aspect ratios (α). The theoretical prediction of $V_{SH}(\varphi = 0^\circ)$ (green curve) using the crack porosity of equation 2.6, shows a good agreement with experimental

Table 4.1: Experimental P- and S-wave velocities for dry condition.

Sample	$V_{P0^\circ}^{dry} (m/s)$	$V_{P45^\circ}^{dry} (m/s)$	$V_{P90^\circ}^{dry} (m/s)$	$V_{SH}^{dry} (m/s)$	$V_{SV}^{dry} (m/s)$
Reference	4194	4231	4260	2267	2159
$\alpha_1 \epsilon_1$	4102	4171	4257	2265	2146
$\alpha_1 \epsilon_2$	4032	4155	4254	2264	2137
$\alpha_1 \epsilon_3$	3997	4134	4251	2262	2134
$\alpha_1 \epsilon_4$	3938	4102	4250	2258	2122
$\alpha_2 \epsilon_1$	4079	4165	4256	2261	2143
$\alpha_2 \epsilon_2$	3983	4116	4253	2258	2131
$\alpha_2 \epsilon_3$	3762	3986	4248	2256	2094
$\alpha_2 \epsilon_4$	3574	3847	4236	2255	2065
$\alpha_3 \epsilon_1$	3985	4123	4259	2256	2128
$\alpha_3 \epsilon_2$	3771	3992	4249	2253	2098
$\alpha_3 \epsilon_3$	3606	3883	4243	2252	2067
$\alpha_3 \epsilon_4$	3431	3769	4237	2252	2031
$\alpha_4 \epsilon_1$	3634	3908	4242	2254	2073
$\alpha_4 \epsilon_2$	3453	3819	4238	2252	2045
$\alpha_4 \epsilon_3$	3305	3689	4231	2251	2019
$\alpha_4 \epsilon_4$	3163	3652	4225	2250	1992

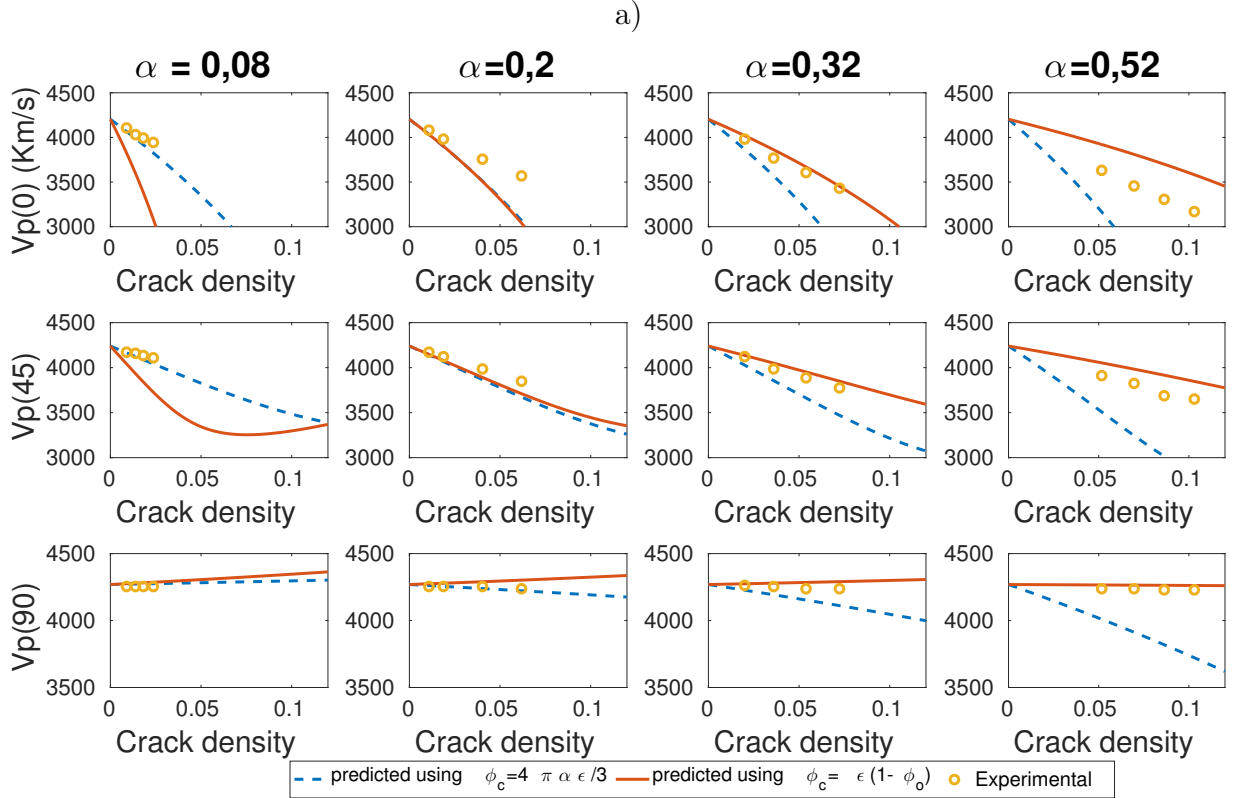


Figure 4.1: P-wave velocities (V_{P0° , V_{P45° and V_{P90°) as function of crack density for different aspect ratios ($\alpha = 0.08, 0.2, 0.32, 0.52$) assuming dry condition. The red circles show the experimental P-wave velocities. The blue and green curves show the P-wave velocities estimated by Eshelby-Cheng model with the crack porosity calculated via equations 2.5 and 2.6, respectively.

results for all crack aspect ratios and crack densities. As can be noted, the predicted velocity (blue curve) using equation 2.5 for the crack and effective porosity shows an underdetermination relative to the experimental values. This behavior can be related to anomalous decreasing of ρ_{total}^{eff} (see Figure 2.2) due to increase of theoretical effective porosity, as shown in Figure 4.3, as the crack density and aspect ratio increase. As expected, the theoretical and experimental S-wave velocities related to the polarization perpendicular to the crack plane decreases as aspect ratio and crack density increase. This behavior was observed by Henriques et al. (21) for cracked models made using epoxy resin and rubber penny-shaped inclusions.

As it was observed for P-wave velocities, in general the S-wave velocity predictions show acceptable fitting with experimental values, in two regimes of crack aspect-ratios: 0.08 and 0.2. For 0.08 and 0.2, the theoretical predictions show best fitting when the crack porosity is given by equation 2.5 and for crack aspect ratio of 0.32 and 0.52, the best prediction occurs when the model is fed by the crack porosity of the equation 2.6. By observing equation 2.5, we can infer that small crack aspect ratios ($\alpha < 0.1$), i. e. thin cracks, need to be geometrically specified by the aperture and length and for higher aspect-ratio cracks, it loses the physical sense of very thin cracks.

4.1.2 Thomsen Parameters

Figure 4.4 shows the estimated and measured Thomsen parameters, γ , ε and δ , as function of crack density. From a general point of view, both experimental and theoretical values increase with crack density, for all crack aspect ratios as expected. According to Figure 4.4, the best Thomsen (32)'s parameter predictions occurred for crack aspect ratios 0.08, using equation 2.5 (blue curve), and 0.2 using equations 2.5 and 2.6 (both green and blue curves), both for crack density values smaller than 4 %. For $\alpha = 0.32$ the acceptable agreement between experimental and theoretical comparisons occurred when the crack density was lower than 7 %, using 2.6 (in green line). As observed, in the P and S-wave velocity predictions, there is a performance range of each crack porosity equation. For the crack aspect ratios below 0.2, the estimative based on equation 2.5 is better than the estimative performed using equation 2.6. For crack aspect ratios higher than 0.2 the opposite occurs.

About Thomsen parameters γ and ε , for aspect ratios below 0.32, they were those that presented the best fitting between the experimental values and theoretical predictions. The theoretical prediction of δ parameter as function of crack density shows an unstable behavior related to the increasing of crack aspect ratio (see Figure 4.4). This can be related to the fact that this parameter depends on several variables to be calculated. This unstable behavior also was verified in the δ estimated by Henriques et al. (21). As pointed out by Yan et al. (36), the majority of δ experimental measurements has very

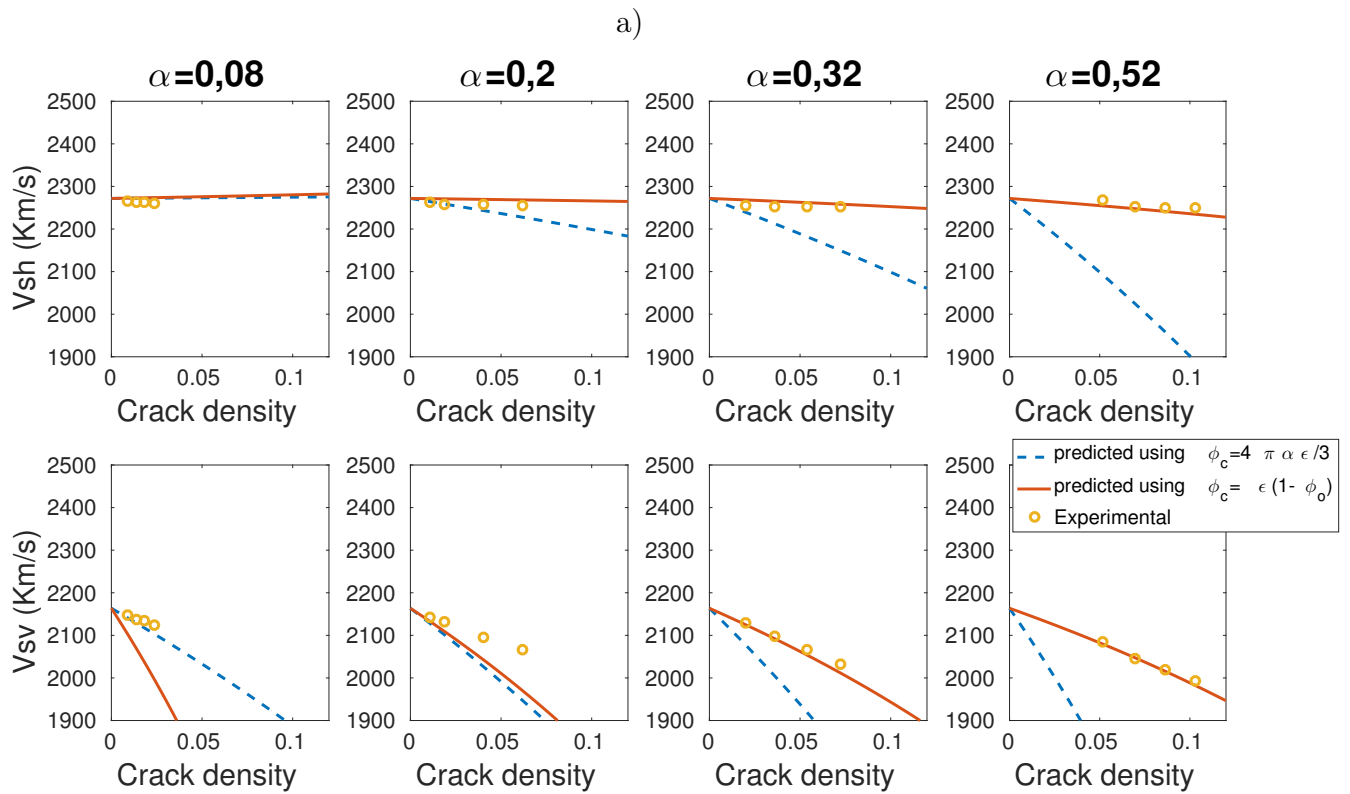


Figure 4.2: S-wave velocities (V_{SH} and V_{SV}) as function of crack density for different aspect ratios ($\alpha = 0.08, 0.2, 0.32, 0.52$) assuming dry condition. The red circles show the experimental S-wave velocities. The blue and green curves show the S-wave velocities estimated by Eshelby-Cheng's model with the crack porosity calculated via equations 2.5 and 2.6, respectively.

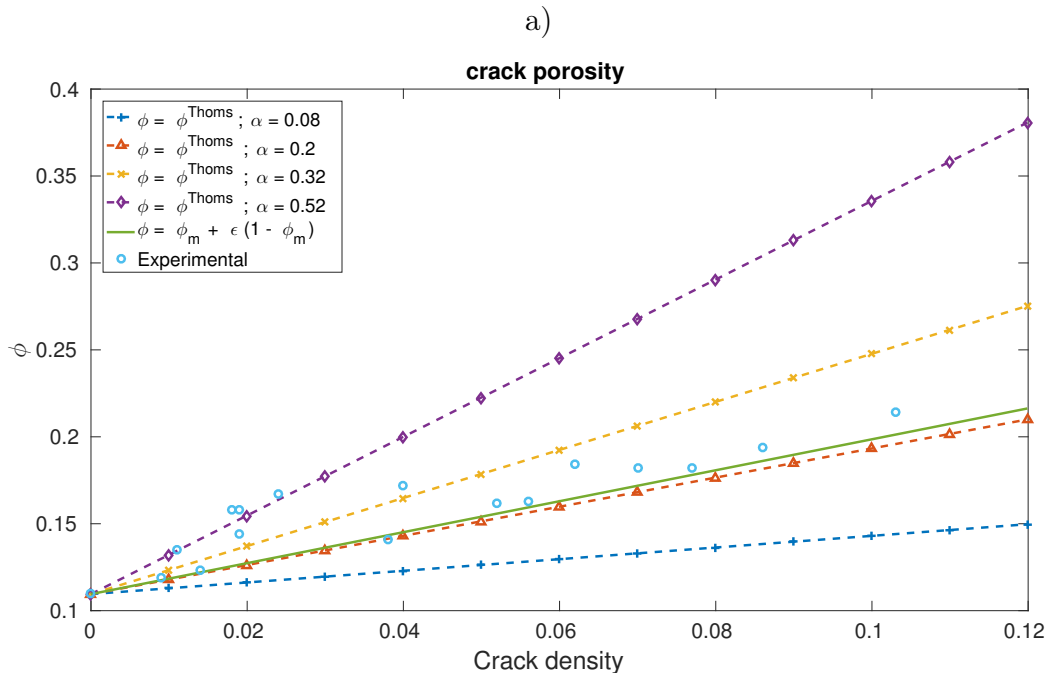


Figure 4.3: The red circles show the experimental crack sample porosities as function of the crack density for the sixteen cracked samples. To estimate the theoretical crack densities we used equations 2.5 and 2.6. The best fit between the estimated and experimental density occurred for theoretical porosity estimated by equation 2.7. Using the Thomsen (33)'s porosity equation, only in case of $\alpha = 0.2$, a reasonable fitting between theory and experiments can be observed.

poor correlation relative to the other Thomsen parameters and a very high uncertainty range.

4.2 ANALYSIS OF MODEL AS A FUCTION OF CRACK ASPECT RATIO

4.2.1 Data interpolation

As there was not possible to acquire experimental data for velocity as function of aspect ratio (for fixed values of crack density), we performed a linear interpolation of the velocities as function of crack density and "resampled" the linear function for fixed values of crack density. As this process is repeated - using the same crack density values for different curves - for the four crack aspect ratios studied, it produces values that approximate how the velocity would change in a sample for varying aspect ratios, maintaining the crack density constant. The linear interpolation was chosen, instead of a higher polinomial fitting, beacuse the velocity values had a small relative rate of change inside the interval considered, as can be seen in Figure 4.5.

The same methodology was applied to the Thomsen parameter's data in order to produce an estimative of the Thomsen parameters as function of aspect ratio, estimative that would not be possible to obtain experimentally, because the Thomsen parameters are

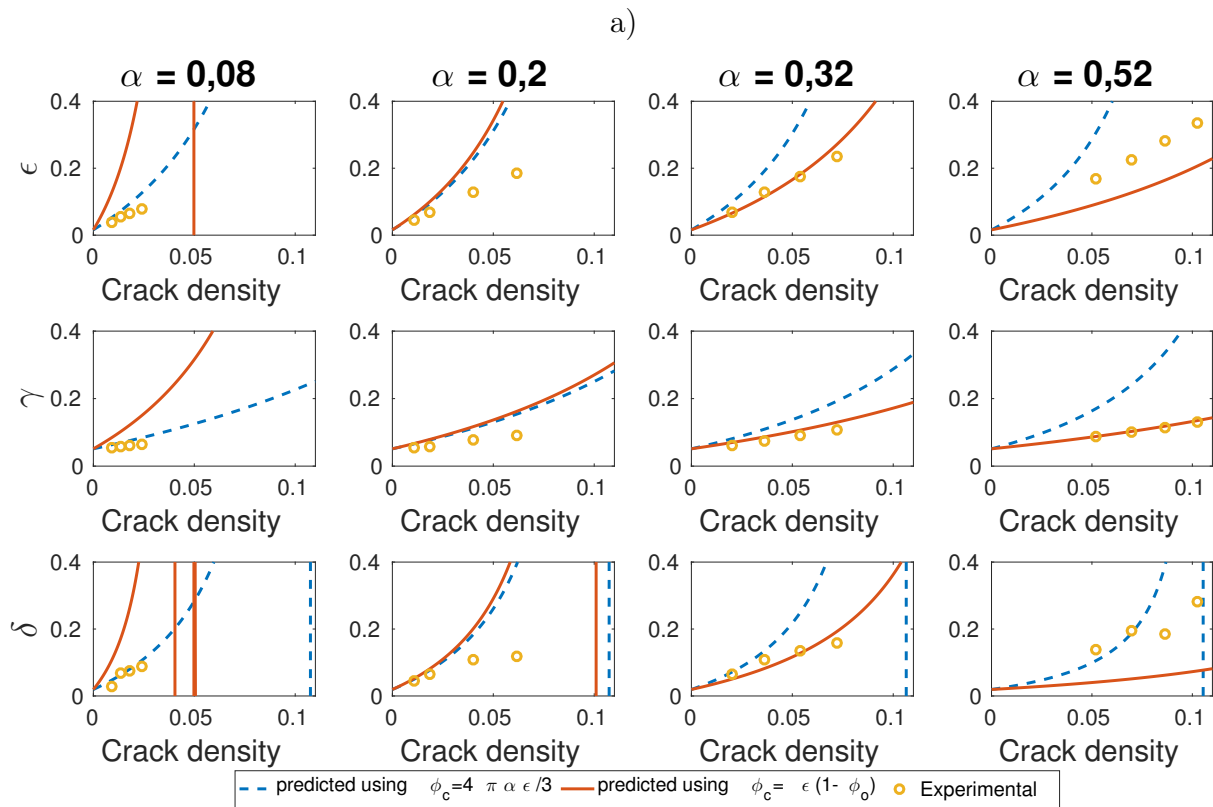


Figure 4.4: Thomsen Parameters (γ , ϵ and δ) as function of crack density for different aspect ratios: $\alpha = 0.08, 0.2, 0.32, 0.52$. The red circles show the Thomsen Parameters obtained from the experimental velocities. The blue and green curves show the Thomsen Parameters obtained from the velocities estimated by Eshelby-Cheng's model with crack porosity calculated using equations 2.5 and 2.6, respectively.

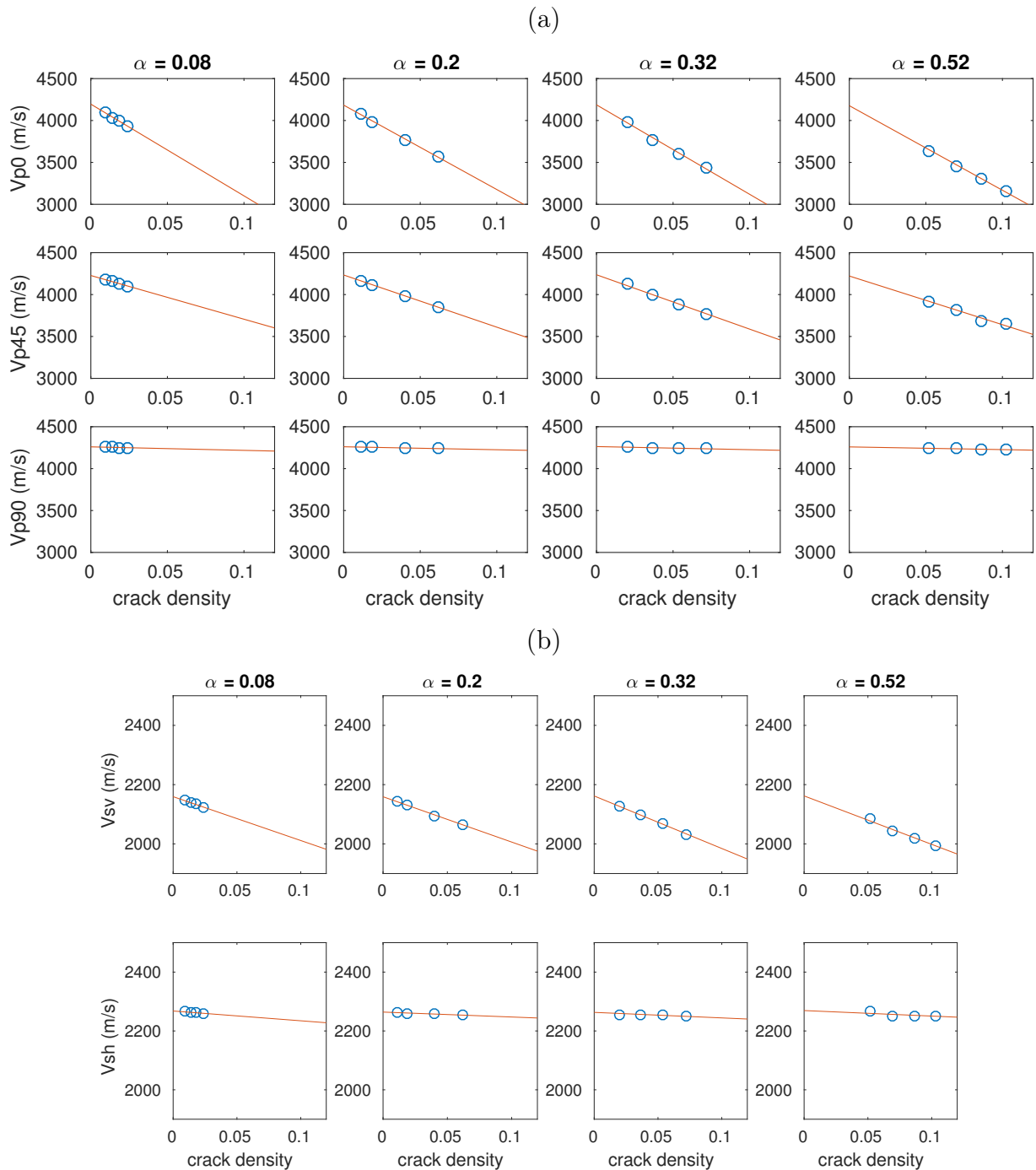


Figure 4.5: Interpolation performed to the velocities as function of crack density in order to produce an estimative of velocities as function of crack aspect ratio. Each column is associated with a fixed value of crack aspect ratio, while each graph shows velocities as function of crack density. The blue circles represent the experimental velocity data. The red lines represent the linear interpolation of the experimental data.

calculated from the five elastic velocities measured, which in turn could be not measured for varying aspect ratios with fixed crack densities, as described earlier. Figure 4.6 shows the Thomsen parameters calculated from the measured velocities as function of crack density for fixed aspect ratios, as well as the linear regression of the data corresponding

to each aspect ratio. Sampling this curves in the same crack density values - noting that each column corresponds to an aspect ratio value - produces the desired estimative: Thomsen parameters as function of cracks aspect ratio with fixed crack densities.

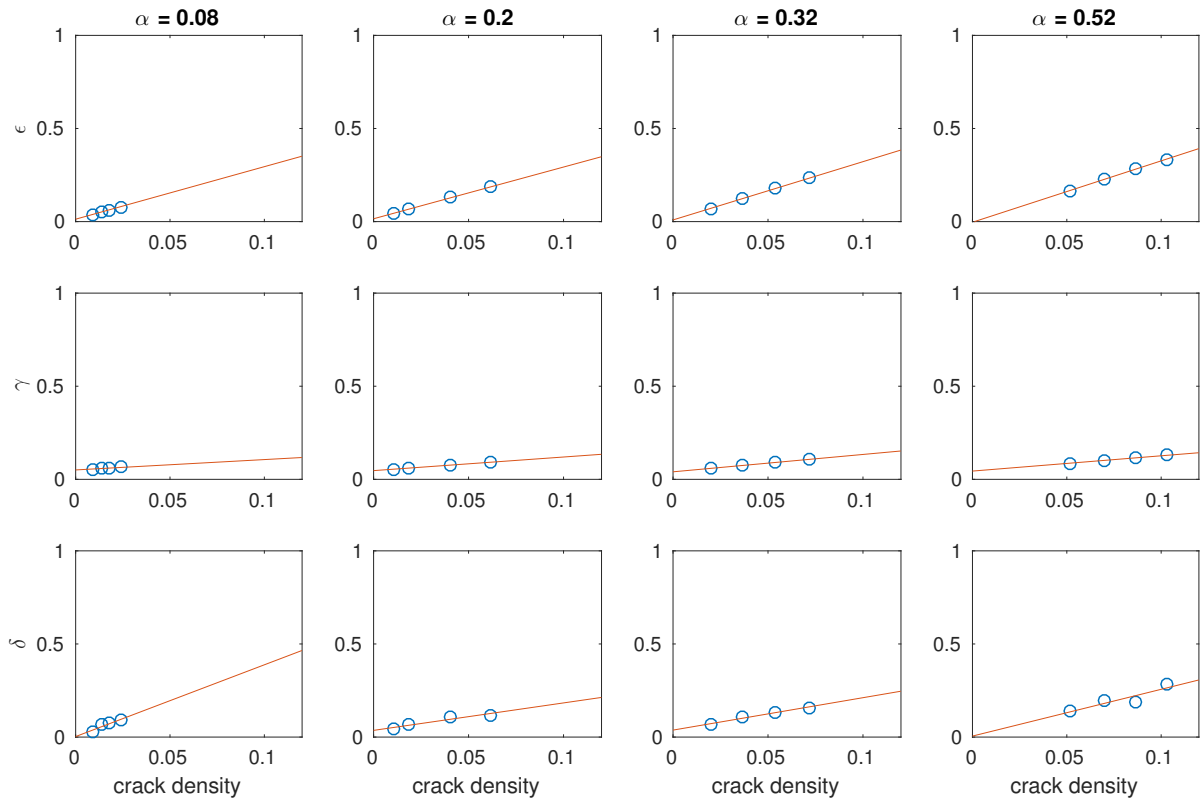
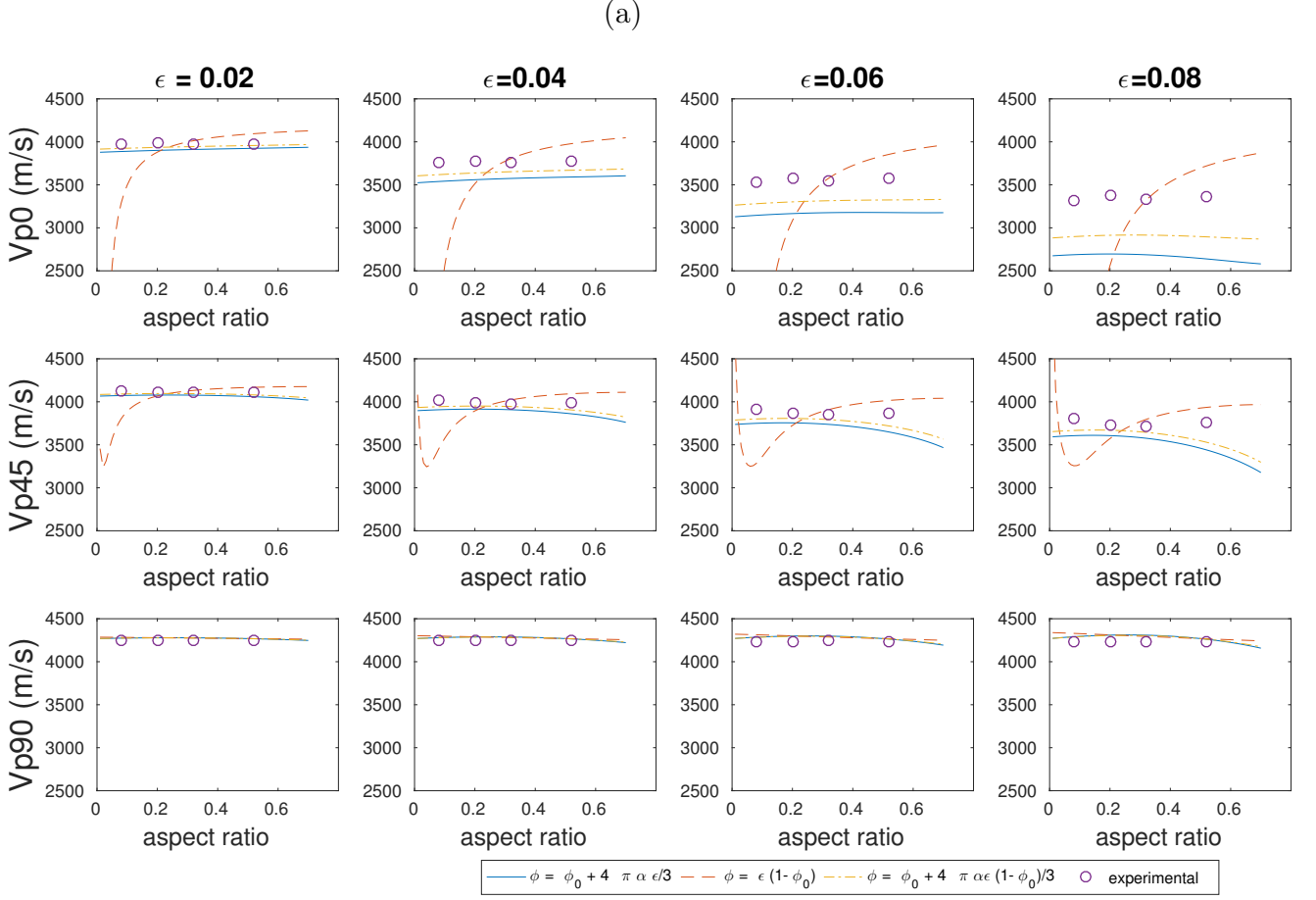


Figure 4.6: Linear regression performed to the Thomsen parameters as function of crack density in order to produce an estimative of Thomsen parameters as function of crack aspect ratio. Each column is associated with a fixed value of crack aspect ratio, while each line of graphs shows a Thomsen parameter as function of crack density. The blue circles represent the Thomsen parameters calculated directly from experimental data. The red lines represent the linear interpolation of the data.

4.2.2 Elastic velocities

The Eshelby-Cheng model, following the workflow adapted for rocks with porous VTI background, was used for the calculations of the curves in Figure 4.7. Differently from the previous work, the theoretical curves for the velocities were calculated as functions of the crack aspect ratio. The purple circles represent the experimental data (or our better estimative of it, given our experimental limitations), that is, the results of the interpolation described in the data interpolation subsection of the methodology section.

The workflow shown in Figure 2.1 was applied for calculating the theoretical elastic velocities, using -as estimative of the crack porosity- equation 2.5 to generate the blue continuous curves, equation 2.6 to generate the dashed red curves and equation 2.9 to



generate the yellow curves made of dashes and points.

It is possible to observe in Figure 4.7 that, in general, the yellow curves follow closer to the circles (i.e., that they have a better fitting with the data) than the other two curves and that the blue curves are just a little further away from the points, while the red curves have a very different behavior from the other two and are much further away from the data circles in some graphs - e.g., Vp_0 , Vp_{45} and V_{sv} plots. The fact that the velocity curves calculated using crack porosity equations 2.5 and 2.9 show a very similar behavior, while the velocities calculated using crack porosity equation 2.6 show a different pattern, can be associated to the fact that in the first pair of equations the crack porosity has an explicit dependence on both crack density and crack aspect ratio (note that the expressions are basically the same function, differing only by a proportionality factor of $(1 - \phi_0)$), while the third crack porosity equation mentioned has an explicit dependence only on crack density.

4.2.3 Thomsen parameters

From the theoretical velocity values (i.e., calculated with the effective medium theory), using equations of Appendix C, the Thomsen Parameters ϵ , δ and γ were calculated, as functions of aspect ratio. As described in the data interpolation subsection in the method-

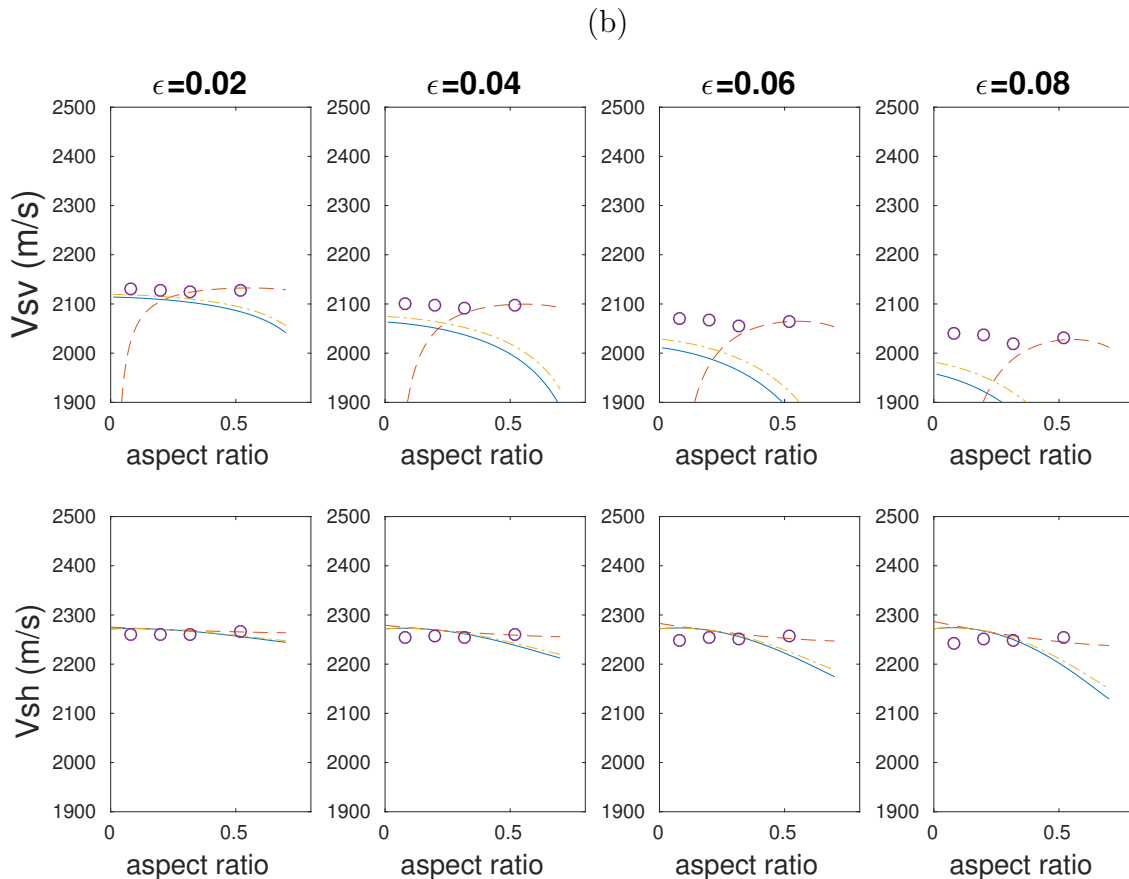


Figure 4.7: The vertical axis shows values of velocity, while the horizontal axis shows values of crack aspect ratio. Each line of graphs shows an elastic velocity with a specific direction of propagation, while each column of graphs is related to a fixed value of crack density. The purple circles represent the velocity values obtained via interpolation of the experimental data. All three curves represent velocity values calculated using the Eshelby-Cheng model workflow shown in Figure 2.1, but the blue continuous curves represent the velocity values calculated using the crack porosity estimated by equation 2.5, while the red dashed curves represent the velocity values calculated using the crack porosity estimated by equation 2.6 and the yellow curves made of dashes and points represent the velocities calculated using the model fed by crack porosity equation 2.9.

ology section, the experimental velocity values were also used to calculate the Thomsen parameters, then these values were interpolated and resampled in order to produce an approximation of the experimental data that would be measured for the Thomsen parameters as function of aspect ratio. The comparisons between the theoretical (calculated from the theoretical velocities, using the three formulations) and the experimental (or an approximation of what would be the experimental values) Thomsen parameters are shown in Figure 4.8.

In Figure 4.8 we observe basically the same features observed in Figure 4.7, that is: the curves associated to the crack porosity equation 2.9 present the best fittings with the data, while the curves associated to the crack porosity 2.5 shows the same pattern following the

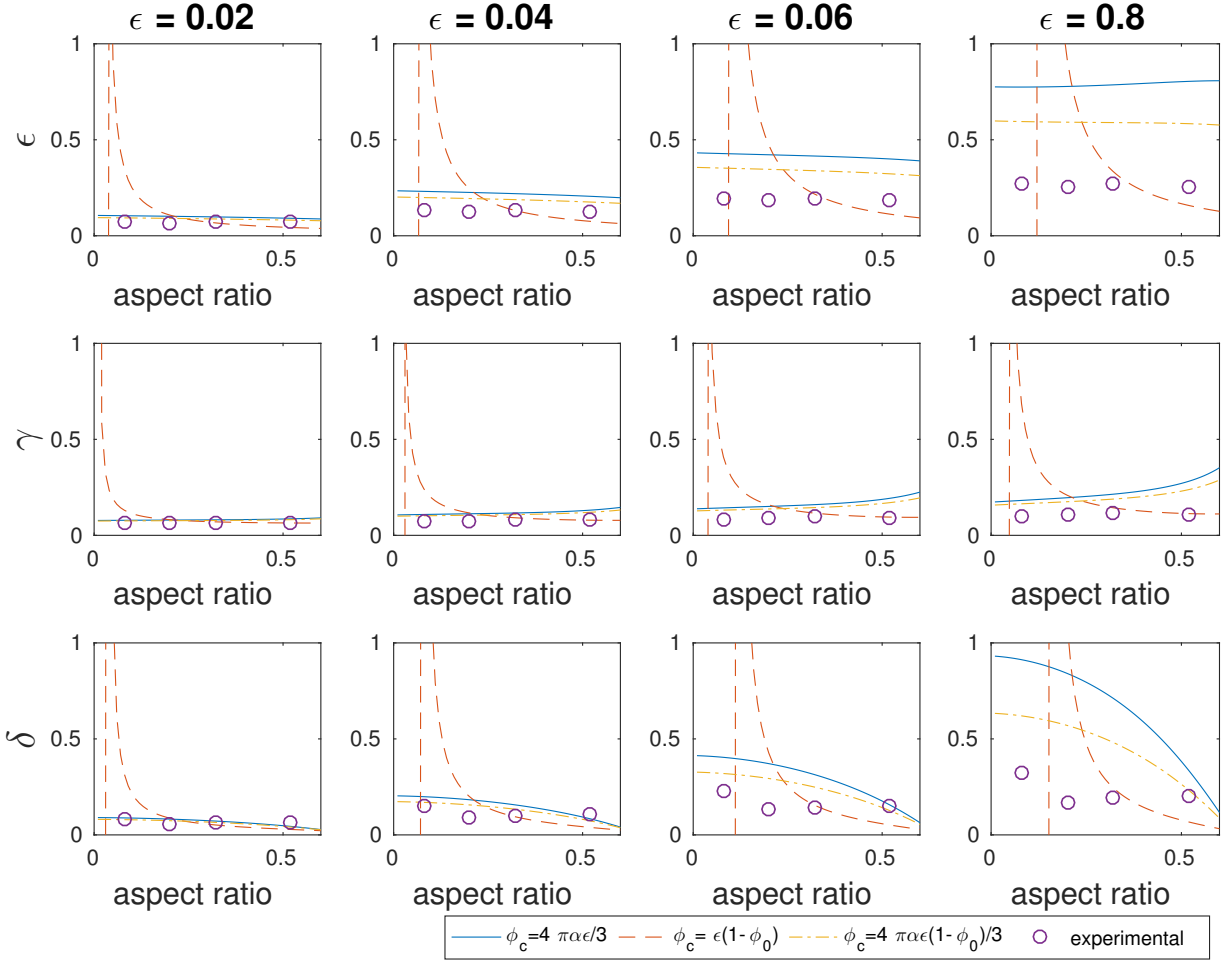


Figure 4.8: The vertical axis shows values of the Thomsen parameters -which are dimensionless and vary always between zero and one- while the horizontal axis shows values of crack aspect ratio. The first line of graphs shows the values for the ϵ parameter (also known as P-wave anisotropy), the second line of graphs shows the values for the γ parameter (also known as P-wave anisotropy) and the third line shows the values for the δ parameter, which is related both to P- and S-waves, while each column is associated to a fixed value of crack density. The purple circles represent the parameters values obtained via interpolation of the experimental data. All three curves represent parameters obtained from velocities calculated using the Eshelby-Cheng model workflow shown in Figure 2.1, but the blue continuous curves represent the velocity values calculated using the crack porosity estimated by equation 2.5, while the red dashed curves represent the velocity values calculated using the crack porosity estimated by equation 2.6 and the yellow curves made of dashes and points represent the velocities calculated using the model fed by crack porosity equation 2.9.

trend of the circles, while being just a little further away from the data points. The curves associated to the crack porosity equation 2.6 show a completely different behavior from the other two, being much further away from the points -and not following the trend of the data- at least for low aspect ratio values. Another problem concerning the red curves (related to the crack porosity 2.6) is that its values seem to not respect the restriction

values of the Thomsen parameters, the curves assume negative values, then increase very fast surpassing one and then come back to reasonable values. Visually, the misfit between the latter mentioned curves and the circles looks greater for low aspect ratio values.

5 DISCUSSIONS

We tested our experimental results against predictions of an effective medium model underinvestigated, Eshelby-Cheng’s model, from an experimental point of view. From a first inspection of P- and S-wave velocities, as well as the anisotropy parameters, we can observe that Eshelby-Cheng’s model provides a better agreement between experimental and theoretical results depending on the crack porosity equation chosen, equation 2.5 or 2.6. One of the limitations of Eshelby-Cheng’s model, besides the homogeneous background assumption, is the requirement of low crack concentrations (lower than 10 %), i. e., no contact between cracks. In case of the foregoing condition being attended Eshelby-Cheng’s model is valid for all crack aspect ratios. However, an advantage of this model (compared with other models, e.g., (22)) is that it can handle all aspect ratios. In this work, we present a validation of the previous statement, even considering a weak anisotropic background, if we allow the crack porosity equation to change according to the range of crack aspect ratios.

As observed by Henriques et al. (21) in an experimental work performed with cracked physical models for crack density sets of 5% and 8%, with six samples for each set, the $V_{P90^\circ}^{dry}$ and V_{SH}^{dry} showed a linear behavior with increasing crack aspect ratio. In this work, we fixed the aspect ratio and changed the crack density. In our case, it is possible to observe that the third curve of Figure 4.1 referring to the $V_{P90^\circ}^{dry}$ and that the second curve of Figure 4.2 referring to the V_{SH}^{dry} seem to be constant with increasing crack aspect ratio. We can infer from the comparison between this and Henriques et al. (21)’s work that these two velocities seem to be independent of crack filling, since the rubber disc inclusions simulate weak-filling materials (21), i. e., saturation different of air.

Another important factor that should be mentioned is the scattering effect. Although the low-pass filter has been applied to all waveforms, the relation between wavelength and crack aperture decrease with increasing crack aspect ratio. According to the corresponding values of crack thickness shown in Table 3.1, the ratio of the smallest wavelength parallel to the crack plane (1.216 cm for S-wave) to the highest crack aperture (0.375 cm) is about 3.24. According to the famous experimental work performed by Marion et al. (24), to observe the effective response of P- and S-waves propagation in anisotropic medium, the dominant wavelength should be at least 10 times higher than the heterogeneity thickness in the medium. However, this low ratio of 3.24 did not influence on the prediction of the γ parameter for the group sample whose aspect ratio is 0.52.

For some velocities (V_{P0° and V_{P45°), which the direction of propagation or polarization is not parallel to the crack plane, the distance between experimental values and the ones predicted by Eshelby-Cheng’s model increases when crack aspect ratio is higher than 0.2 and crack density is higher than 0.07. According to the Cheng (9) and Eshelby (16)’s as-

sumptions, the maximum value for crack density accepted in their approximation is about 10 %. It is feasible to think that such low conformity, related to crack density higher than 0.07, can be justified by the presence of the background anisotropy in all samples (γ about 5 %). We suggest, in further experiments, comparisons between modified conventional effective models, as Hudson (22) and Cheng (9), and effective medium theories that take into account the background anisotropy such as M. Kachanov et al. (23) and Grechka and Kachanov (20).

The results obtained from our four sample sets, with varying crack density for each set, have shown evidence of aspect-ratio-dependent behavior of wave propagation in anisotropic elastic media. The penny-shaped inclusions used in this work simulated ideal cylindrical cracks showing a low shear modulus compared to the surrounding porous matrix. Our experiments used an idealized crack system exhibiting aligned crack distributions with different crack parameters: density and aspect-ratio. The size of the individual cracks was much smaller than the smallest seismic wavelength, at least 4 times. Our results indicate that the velocities as well as Thomsen parameters in such a system depend strongly on the geometric properties of the cracks. Regarding the geometric parameters, crack aperture and crack density were more important than crack diameter as observed in Figueiredo et al. (18). The main point observed here is that elastic waves propagating in different media with different crack geometry features react slightly different to these crack parameters.

This work studies velocities and Thomsen parameters as function of both crack density and aspect ratio - by studying the velocities and Thomsen parameters calculated with the Eshelby-Cheng model as function of aspect ratio, then it is useful to interpret and compare the results obtained in the two analysis from a perspective which treats elastic velocities and anisotropic parameters as multivariable functions of aspect ratio and crack density. Therefore, we calculated and present in Figure 5.1 the velocity maps (we do not present the Thomsen parameters maps because the analysis would be redundant) as function of the two variables discussed here.

It is possible to observe in Figure 5.1 that the velocity maps produced by feeding the Eshelby-Cheng model with crack porosity 2.5 and 2.9 show basically the same contours. That is expected, as the curves (which are essentially profiles of these maps) show very similar behavior and because the porosity equations 2.5 and 2.9 are basically the same functions, differing by a proportionality factor. The velocity maps associated to the crack porosity equation 2.6 has different contours from the other two maps in each elastic velocity, as expected, because its porosity dependency is different from the other two, it depends only on aspect ratio. The velocity maps associated to equation 2.6 show some problems: the Vp_0 and Vsv maps have some regions -low aspect ratio and high crack density regions- in which the model breaks down, that is, produces unphysical results, in this case it produces complex-valued velocity values. That is, probably, due to the fact

that the crack porosity lacks the dependence on the aspect ratio variable (and that analysis was one of our motivations to propose crack porosity equation 2.9, an equation which tries to take into account the background porosity and has the same linear dependencies as equation 2.5).

The curves of velocity as function of crack density can be seen as vertical profiles of the maps presented in Figure 5.1, while the curves of velocity as function of aspect ratio can be seen as horizontal profiles of these maps. Therefore both perspectives compare profiles of these maps to experimental data, but de Figueiredo et al. (12) compares crack porosities 2.5 and 2.6, while this work includes a third formulation and compares it to the previous two. de Figueiredo et al. (12) results shows that the fitting between the model and the data -for velocities as function of crack density- is, in general, better using crack porosity equation 2.5 for lower aspect ratio values, while it is better using crack porosity equation 2.6 for higher aspect ratios. A similar effect can be seen in our results mainly in Figure 4.7 (b), but (as will be demonstrated) the overall errors in these windows related to the crack porosity 2.6 are still greater than the ones related to the crack porosity equation 2.5.

In order to ensure a more rigid analysis in terms of comparisons between the results, we calculated the root-mean-squared (RMS) relative error between theoretical values (elastic velocities and Thomsen parameters calculated using the Eshelby-Cheng model) and experimental data, for each graph shown in Figures 4.7 and 4.8. As the RMS error is calculated adding differences (the squares of the relative differences and then taking the square-root to be more precise) between the curve and the data points along the entire range of aspect ratio, then it is a measure related to the entire curve, so it is useful to solve the issue raised in the previous paragraph (comparing curves that fits better the data in different regions). Each plot is associated to a crack density, therefore the RMS error shown in Figure 5.2 is a function of crack density.

In Figure 5.2 it is possible to observe that the error increases with crack density for all formulations. The distance between data points and calculated curves increases with crack density in the comparison plots shown both in this work and in de Figueiredo et al. (12), so this is further demonstration that all formulations proposed have a limitation concerning high crack density values, differently from their behavior relative to crack aspect ratio, which is different for each formulation: equation 2.6 produces velocities that behave better for high crack aspect ratios and gets worse until it breaks down for low aspect ratios (as discussed earlier), while values related to equation 2.5, as in Figure 4.7 for example, seem to get further away from data points as aspect ratio increases.

In all graphs of Figure 5.2 it is clear that the errors associated to the velocities calculated from the Eshelby-Cheng model with crack porosity equation 2.6 are the greatest, much higher than the other ones, as anticipated by the analysis of Figure 4.7. As clear as the previous observation is noting that the smaller error in all graphs is the one related

to the use of crack porosity equation 2.9, also as anticipated by the analysis of Figure 4.7. The RMS-errors were also calculated for the Thomsen parameters and are shown in Figure 5.3. As the errors associated to the crack porosity equation 2.6 surpassed 100%, they were normalized based on the greatest error in each graph. Therefore it is not possible to draw comparisons of the errors between different parameters, but that is not our goal here.

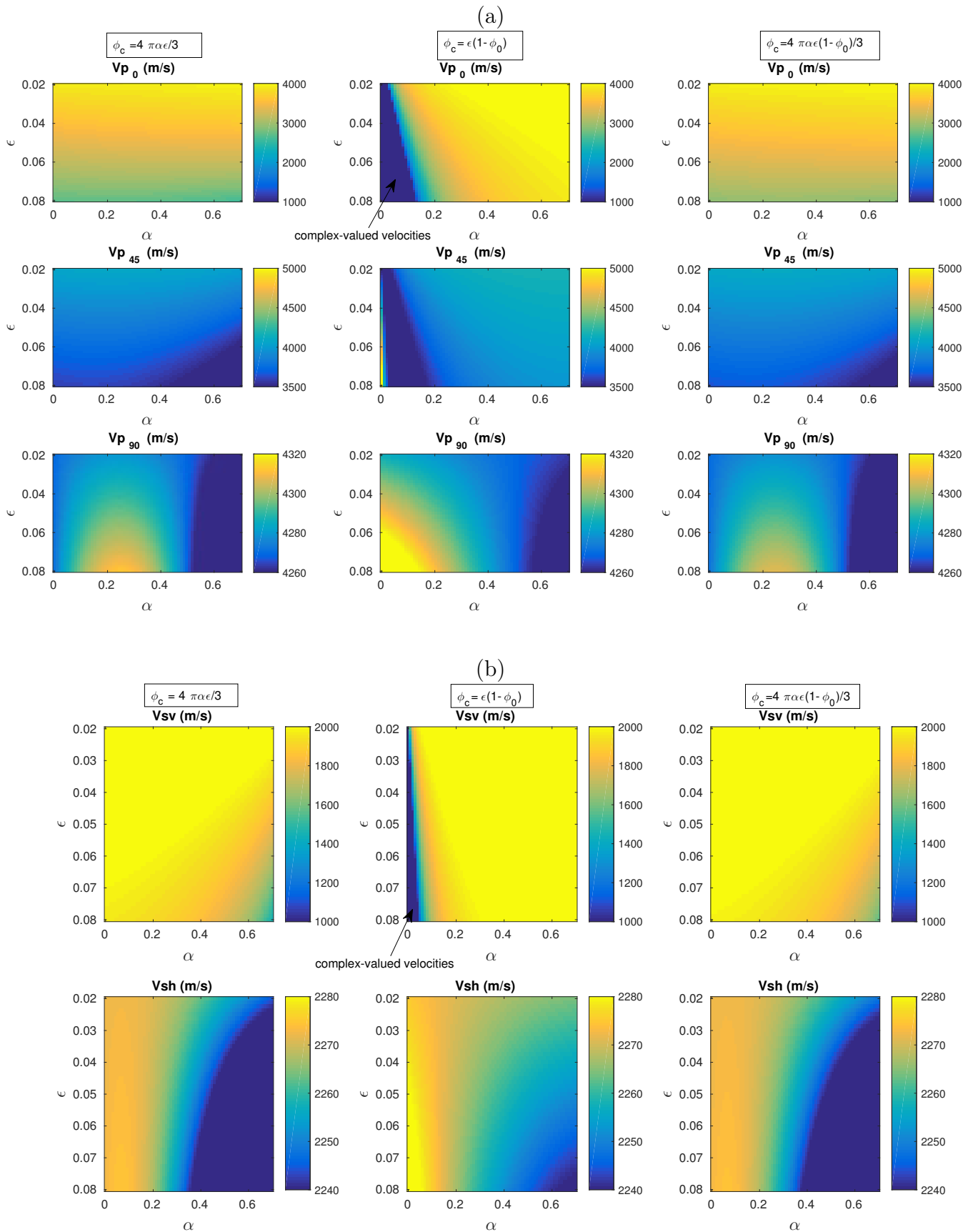


Figure 5.1: Velocity maps produced using Eshelby-Cheng effective medium theory. The colors represent the velocity values in m/s . the vertical axis shows values of crack density, while the horizontal axis shows values of aspect ratio. Each line of maps shows one of the five elastic velocities studied in this work. Each column of maps is associated with one of the three crack porosity equations tested in this work. There are some regions in the maps (first line, second column and fourth line, second column) in which the model, using the Eshelby-Cheng theory, predicts a velocity that is unphysically low.

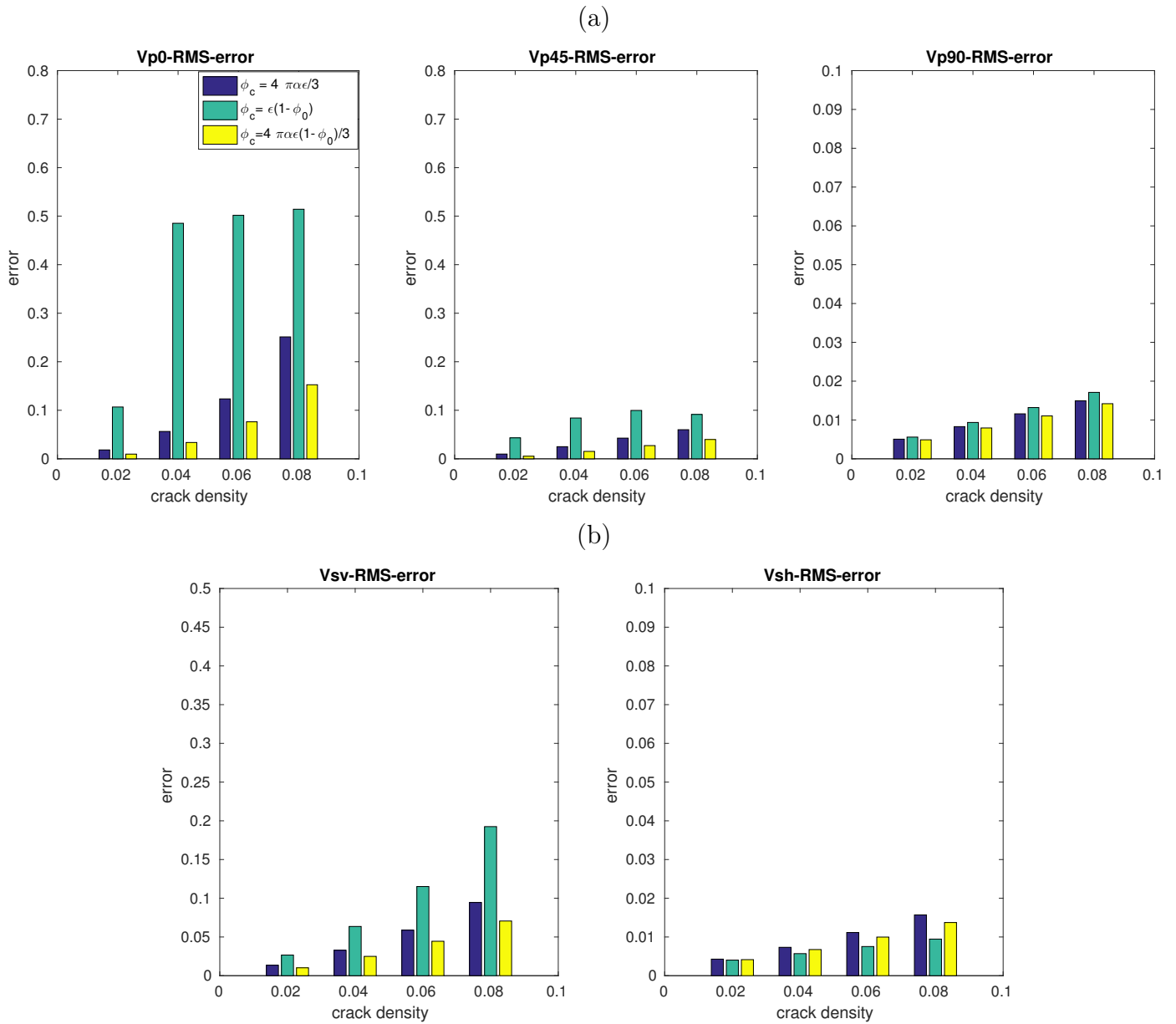


Figure 5.2: Root-mean-squared error between elastic velocities calculated from the Eshelby-Cheng model, using the three crack porosity formulations, and experimental elastic velocities. The errors are shown for each fixed crack density associated to the graph from which the velocity errors were calculated. (a) P-wave velocity errors. (b) S-wave velocity errors.

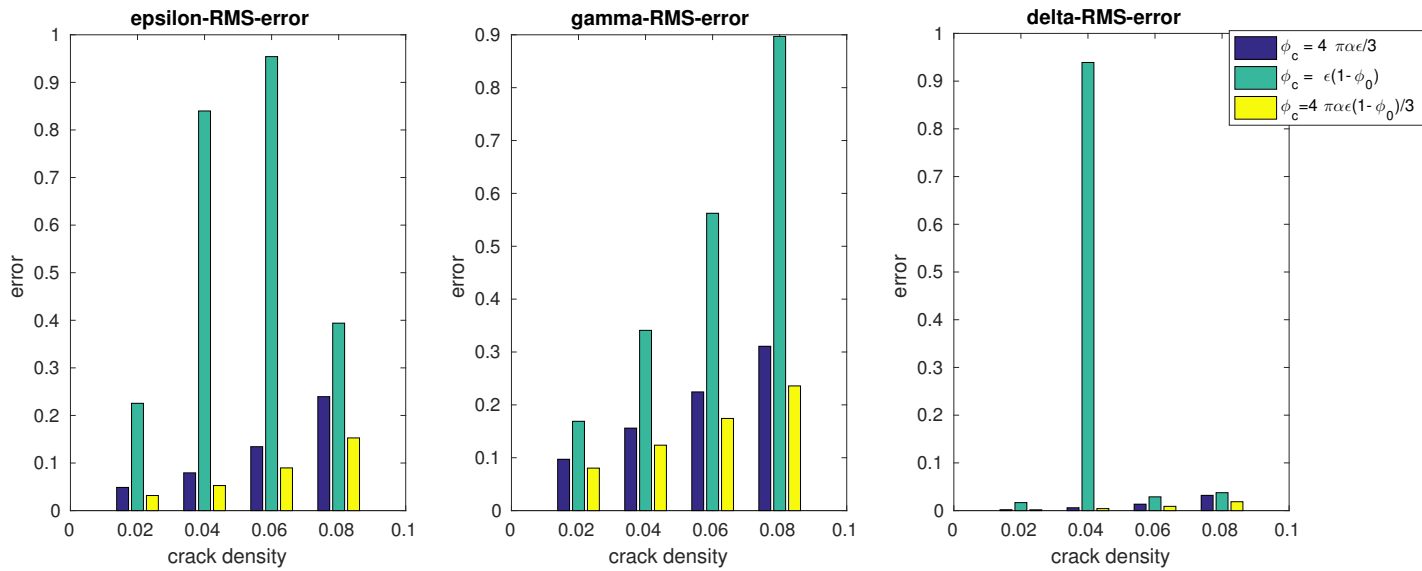


Figure 5.3: Root-mean-squared error between Thomsen parameters calculated from the Eshelby-Cheng model, using the three crack porosity formulations, and experimental elastic velocities. The errors are shown for each fixed crack density associated to the graph from which the anisotropic parameter errors were calculated.

6 CONCLUSIONS

This work was performed in order to test the efficiency of Eshelby-Cheng's model for predicting elastic velocities and Thomsen parameters in cracked samples with weakly anisotropic VTI background. More specifically, we would like to observe how well the predictions of the model would perform for different ranges of crack densities and different aspect ratios. Based on our results we can conclude for crack density analysis:

- (1) Even applying the Eshelby-Cheng's model for samples with weakly VTI anisotropic background, we achieved good agreement between experimental results and the model's predictions, for certain ranges of crack density and aspect ratio.
- (2) in general, Eshelby-Cheng's equations were more prominent on predicting elastic velocities and Thomsen parameters for low crack densities: < 0.07 .
- (3) For different aspect ratios, the performance of the model depends on the porosity equation chosen to feed the model. For low crack aspect ratios (< 0.2) the crack porosity equation proposed by Thomsen (33) works best, while for high crack aspect ratios (> 0.2) equation 9 presents better results.

And for aspect ratio analysis:

- (1) In case of aspect-ratio analysis, the workflow for applying the Eshelby-Cheng model adapted to porous anisotropic cracked samples works best (produces the overall best fitting with the data) when fed with the crack porosity calculated from equation Thomsen (33) modified.
- (2) When fed with crack porosities calculated from our proposed equation, the model produces the worst fittings, mainly for low aspect ratio regions, and is unstable -producing unphysical results- in regions of low aspect ratio and high crack density for the elastic velocities V_{p0} and V_{sv} . This behavior may have a relationship to the fact that equation our proposed equation does not have the original dependence between crack porosity and cracks aspect ratio.
- (3) For all three formulations tested, the RMS error grows with crack density, but for the model fed with the crack porosity equation Thomsen (33) modified the error keeps below 10%, except for V_{p0} when the crack density is the highest tested (0.08).

Considering the fact that this approach leads to good results for cracked media which has weakly VTI background anisotropy, it is possible to argue that our approach is applicable and a good approximation for certain reservoirs, since most of natural rocks exhibit a VTI background anisotropy, due to their layering, and also exhibit oriented crack planes, due to tectonic stresses or induced fracturing.

One limitation is that this work studies sets of cracks oriented parallel to the background medium isotropic planes and not in any arbitrary orientation, that would restrict the use of this approach, making it not applicable to characterize media in which crack planes are

tilted with respect to the isotropic planes of the background.

A generalization, that we suggest as a future work, would be to perform experimental work to study effective medium theories for describing orthorhombic media, which is a good approximation for a medium that has sets of crack planes oriented perpendicular to the background medium layering. Furthermore, we suggest the use of other effective models based on compliance instead of stiffness.

7 APPENDIX

7.1 APPENDIX A- P- AND S-WAVEFORMS

The analysis of this work started with analysis of the transmission waveforms for the reference sample (uncracked), and then the waveforms of all anisotropic cracked samples. When the P-wave and S-wave propagate through the samples the waveform suffers dispersion due to scattering, as observed by (18). To eliminate the coda related to the scattering, a band-pass filter of 100-150-220-280 kHz is applied in the P- and S-wave waveforms to eliminate the coda wave related to scattering. for this dominant frequency (185 kHz) the P- and S-wavelengths range from 2.37 to 1.37 cm and 1.27 to 1.08 cm.

Figure 7.1 show the P- and S-waveforms of reference sample for dry condition. As it can be noted, for both P- and S-wave, there are a difference of first traveltime arrival changing direction of propagation (P-wave) as well as changing the polarization (S-wave). Figures 7.2 and 7.3 show example of P- and S-waveforms for cracked sample in the dry condition. Here, even in the presence of inclusions (in the samples), the quality of seismograms remains high. This characteristics allows us to perform the first arrival picking (for both modes of propagation) with reduced margin of error.

7.2 APPENDIX B- ESHELBY-CHENG EFFECTIVE MODEL

Here, in this work, for limitations related to saturation equipment in the laboratory, we compared the Eshelby-Cheng's effective with experimental results only in dry condition. However, for extension, in this section we show the mathematical formulation of the Eshelby-Cheng's effective model for both dry and saturated condition. According to Eshelby-Cheng's effective model, the C_{ij}^{eff} for a rock containing weak-fluid filled ellipsoidal cracks, can be evaluated by:

$$C_{ij}^{dry,sat(eff)} = C_{ij}^{dry,sat(0)} - \phi C_{ij}^{(dry,sat)-(1)}, \quad (7.1)$$

where

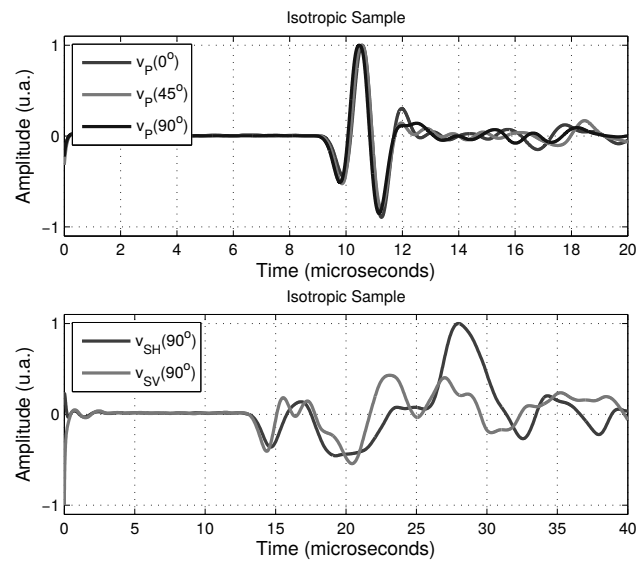


Figure 7.1: (a) P- and (b) S-waveforms for reference sample in dry condition.

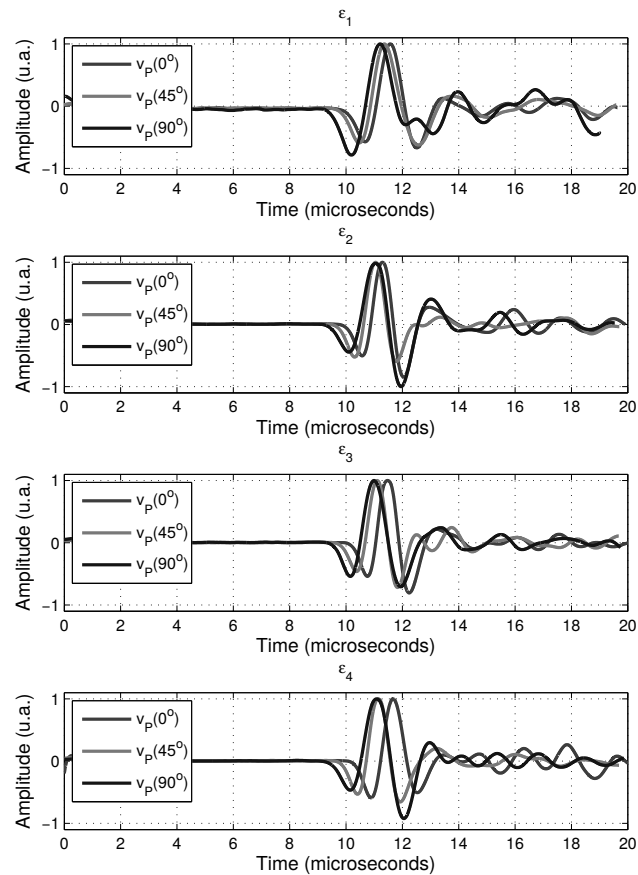


Figure 7.2: P-wave seismograms for samples with aspect ratio $\alpha_1 = 0.08$ in dry condition.

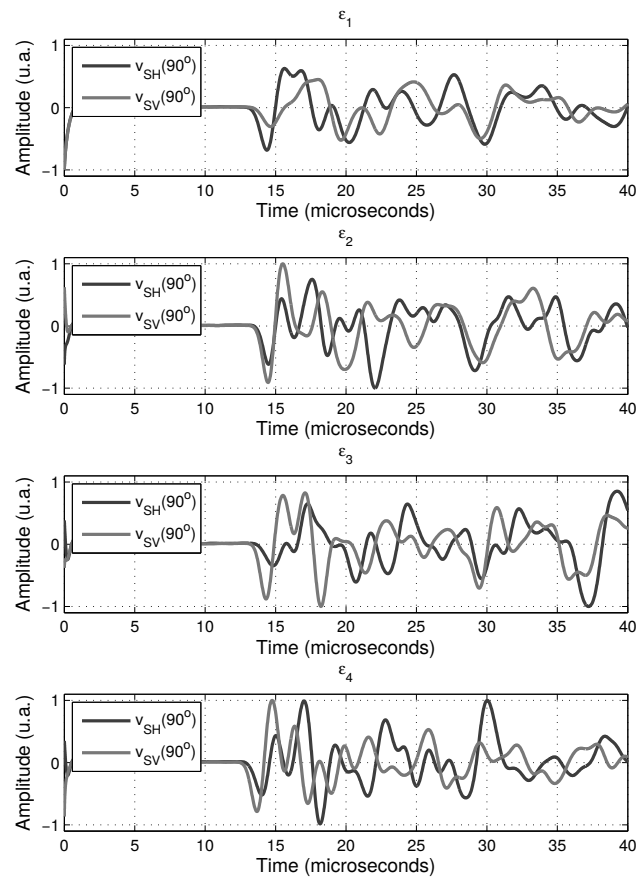


Figure 7.3: S-wave seismograms for samples with aspect ratio $\alpha_1 = 0.08$ in dry condition.

$$\begin{aligned}
c_{11}^1 &= \lambda^{(dry,sat)}(S_{31} - S_{33} + 1) + \frac{2\mu^{(dry,sat)}(S_{33}S_{11} - S_{31}S_{13} - (S_{33} + S_{11} - 2C - 1) + C(S_{31} + S_{13} - S_{11} - S_{33}))}{D(S_{12} - S_{11} + 1)}, \\
c_{33}^1 &= \frac{(\lambda^{(dry,sat)} + 2\mu^{(dry,sat)})(-S_{12} - S_{11} + 1) + 2\lambda^{(dry,sat)}S_{13} + 4\mu^{(dry,sat)}C}{D}, \\
c_{13}^1 &= \frac{(\lambda^{(dry,sat)} + 2\mu^{(dry,sat)})(S_{13} + S_{31}) - 4\mu^{(dry,sat)}C + \lambda^{(dry,sat)}(S_{13} - S_{12} - S_{11} - S_{33} + 2)}{2D}, \\
c_{44}^1 &= \frac{\mu^{(dry,sat)}}{1 - 2S_{1313}}, \\
c_{66}^1 &= \frac{\mu^{(dry,sat)}}{1 - 2S_{1212}},
\end{aligned}$$

$$\begin{aligned}
S_{11} &= QI_{\alpha\alpha} + RI_{\alpha}, \\
S_{33} &= Q\left(\frac{4\pi}{3} - 2I_{\alpha c}\alpha^2\right) + I_cR, \\
S_{12} &= QI_{\alpha b} - RI_{\alpha}, \\
S_{13} &= QI_{\alpha c}\alpha^2 - RI_{\alpha}, \\
S_{31} &= QI_{\alpha c} - RI_c, \\
S_{1212} &= QI_{\alpha b} + RI_{\alpha}, \\
S_{1313} &= \frac{Q(1 + \alpha^2)I_{\alpha c}}{2} + \frac{R(I_{\alpha} + I_c)}{2},
\end{aligned}$$

$$\begin{aligned}
I_{\alpha} &= \frac{2\pi\alpha(\cos^{-1}\alpha - \alpha S_{\alpha})}{S_{\alpha}^3}, \\
I_c &= 4\pi - 2I_{\alpha}, \\
I_{\alpha\alpha} &= \pi - (3/4)I_{\alpha c}, \\
I_{\alpha c} &= \frac{I_c - I_{\alpha}}{3S_{\alpha}^3}, \\
I_{\alpha b} &= \frac{I_{\alpha\alpha}}{3},
\end{aligned}$$

$$\begin{aligned}
S_\alpha &= \sqrt{1 - \alpha^2}, \\
\sigma &= \frac{3K^{(dry,sat)} - 2\mu^{(dry,sat)}}{6K + 2\mu^{(dry,sat)}}, \\
R &= \frac{1 - 2\sigma}{8\pi(1 - \sigma)}, \\
Q &= \frac{3R}{1 - 2\sigma}, \\
C &= \frac{k_f}{3(K^{(dry,sat)} - k_f)}, \\
I &= K^{(dry,sat)} - \frac{2\mu^{(dry,sat)}}{3},
\end{aligned}$$

where α is the crack aspect ratio, $K^{(dry,sat)}$ is the bulk modulus of solid matrix, k_f (0.0 GPa and 2.2 GPa for air and water, respectively) is the fluid bulk modulus. The $\lambda^{(dry,sat)}$ and $\mu^{(dry,sat)}$ are the Lamé parameters for dry or water saturated reference sample (matrix without inclusions), respectively. According to the flowchart showed in Figure 2.1, the reference bulk and shear modulus are

$$K^{dry,sat} = \rho^{dry,sat} \left((V_{P0}^{dry,sat})^2 + \frac{4}{3}(V_{S0}^{dry,sat})^2 \right), \quad (7.2)$$

$$\mu^{(dry,sat)} = \rho^{dry,sat} (V_{S0}^{dry,sat})^2. \quad (7.3)$$

7.3 APPENDIX C-EFFECTIVE THOMSEN PARAMETER

Figure 2.1 shows a flowchart with the "ingredients" used to feed the modified Eshelby-Cheng's model. As our reference sample is not isotropic, to feed the Eshelby-Cheng's model, we used ρ^{ref} (see Table 3.1), $V_{P0} = (V_P^{ref}(\theta = 0^\circ) + V_P^{ref}(\theta = 90^\circ))/2$, $V_{S0} = (V_S^{ref}(\varphi = 0^\circ) + V_S^{ref}(\varphi = 90^\circ))/2$ (see Table 4.1). The output of model (see branch (2) of flowchart) are elastic coefficient constant as function of crack parameter (ϵ, α). These coefficients can be converted in velocities using equations such as

$$V_{P,S}^{eff(dry,sat)} \propto \sqrt{\frac{C_{ij}^{eff(dry,sat)-mod}}{\rho_{eff}^{(dry,sat)}}}, \quad (7.4)$$

where ρ_{eff} the the theoretical effective density shown in the flowchart of Figure 2.1. Specifically, the effective velocities (dry and/or sat) as well as the effective Thomsen

parameters (also dry and/or sat) can be estimated by the following equations:

$$C_{11}^{eff} = \rho^{eff} (V_P^2(\theta = 90^\circ))^{eff} \quad (7.5)$$

$$C_{33}^{eff} = \rho^{eff} (V_P^2(\theta = 0^\circ))^{eff} \quad (7.6)$$

$$C_{44}^{eff} = \rho^{eff} (V_{S2}^2(\varphi = 90^\circ))^{eff} \quad (7.7)$$

$$C_{66}^{eff} = \rho^{eff} (V_{S1}^2(\varphi = 0^\circ))^{eff} \quad (7.8)$$

$$C_{13}^{eff} = \left[\frac{\left(4\rho^{eff} (V_P^2(\theta = 45^\circ))^{eff} - C_{11}^{eff} - C_{33}^{eff} - 2C_{44}^{eff} \right)^2 - \left(C_{11}^{eff} - C_{33}^{eff} \right)^2}{4} \right]^{\frac{1}{2}} - C_{44}^{eff}$$

with

$$C_{12}^{eff} = C_{11}^{eff} - 2C_{66}^{eff}, \quad (7.10)$$

and

$$\gamma^{eff} = \frac{C_{66}^{eff} - C_{44}^{eff}}{2C_{44}^{eff}}, \quad (7.11)$$

$$\varepsilon^{eff} = \frac{C_{11}^{eff} - C_{33}^{eff}}{2C_{33}^{eff}}, \quad (7.12)$$

$$\delta^{eff} = \frac{(C_{13}^{eff} + C_{44}^{eff})^2 - (C_{33}^{eff} - C_{44}^{eff})^2}{2C_{33}^{eff} (C_{33}^{eff} - C_{44}^{eff})}. \quad (7.13)$$

BIBLIOGRAPHY

- [1] Amalokwu, K., M. Chapman, A. I. Best, T. A. Minshull, and X.-Y. Li, 2015, Water saturation effects on P-wave anisotropy in synthetic sandstone with aligned fractures: *Geophysical Journal International*, **202**, 1088–1095.
- [2] Assa'd, J., R. Tatham, and J. McDonald, 1992, A physical model study of microcrack-induced anisotropy: *Geophysics*, **57**, 1562–1570.
- [3] Assa'd, J. M., R. H. Tatham, J. A. McDonald, T. M. Kusky, and J. Jech, 1993, A Physical Model Study of Scattering of Waves by Aligned Cracks: Comparison Between Experiment and Theory1: *Geophysical Prospecting*, **41**, 323–339.
- [4] Bakulin, A., V. Grechka, and I. Tsvankin, 2000a, Estimation of fracture parameters from reflection seismic data—Part III: Fractured models with monoclinic symmetry: *Geophysics*, **65**, 1818–1830.
- [5] ———, 2000b, Estimation of fracture parameters from reflection seismic data—Part III: Fractured models with orthorhombic symmetry: *Geophysics*, **65**, 1803–1817.
- [6] Boadu, F. K., and L. T. Long, 1996, Effects of fractures on seismic-wave velocity and attenuation: *Geophysical Journal International*, **127**, 86–110.
- [7] Bonafede, M., B. Parenti, and E. Rivalta, 2002, On strike-slip faulting in layered media: *Geophysical Journal International*, **149**, 698–723.
- [8] Chapman, M., 2013, frequency-dependent anisotropy due to meso-scale fractures in the presence of equant porosity: *Geophysical Prospecting*, **51**, 369–379.
- [9] Cheng, C. H., 1993, Crack models for a transversely isotropic medium: *Journal of Geophysical Research: Solid Earth*, **98**, 675–684.
- [10] Crampin, S., and S. Chastin, 2003, A review of shear wave splitting in the crack-critical crust: *Geophysical Journal International*, **155**, 221–240.
- [11] Crampin, S., and S. Peacock, 2005, A review of shear-wave splitting in the compliant crack-critical anisotropic Earth: *Wave Motion*, **41**, 59–77.
- [12] de Figueiredo, J. J. S., M. J. do Nascimento, E. Hartmann, B. F. Chiba, C. B. da Silva, M. C. De Sousa, C. Silva, and L. K. Santos, 2018, On the application of the eshelby-cheng effective model in a porous cracked medium with background anisotropy: An experimental approach: *Geophysics*, **83**, C209–C220.
- [13] De Figueiredo, J. J. S., J. Schleicher, R. R. Stewart, and N. Dyaur, 2012, Estimating fracture orientation from elastic-wave propagation: An ultrasonic experimental approach: *Journal of Geophysical Research: Solid Earth*, **117**, B08304.
- [Dellinger and Vernik] Dellinger, J., and L. Vernik, : *Geophysics*, 1774–1779.
- [15] Ding, P., B. Di, D. Wang, J. Wei, and X. Li, 2014, P and S wave anisotropy in fractured media: Experimental research using synthetic samples: *Journal of Applied Geophysics*, **109**, 1–6.
- [16] Eshelby, J. D., 1957, The determination of the elastic field of an ellipsoidal inclusion,

- and related problems: *Proc. Roy. Soc. London*, **241**, 376–396.
- [17] Far, M. E., C. M. Sayers, L. Thomsen, D.-h. Han, and J. P. Castagna, 2013, Seismic characterization of naturally fractured reservoirs using amplitude versus offset and azimuth analysis: *Geophysical Prospecting*, **61**, 427–447.
- [18] Figueiredo, D., J. J. S. de Figueiredo, J. Schleicher, R. R. Stewart, N. Dayur, B. Omoboya, R. Wiley, and A. William, 2013, Shear wave anisotropy from aligned inclusions: ultrasonic frequency dependence of velocity and attenuation: *Geophysical Journal International*, **193**, 475–488.
- [19] Grechka, V., 2007, Multiple cracks in VTI rocks: Effective properties and fracture characterization: *Geophysics*, **72**, D81–D91.
- [20] Grechka, V., and M. Kachanov, 2006, Effective elasticity of rocks with closely spaced and intersecting cracks: *Geophysics*, **71**, D85–D91.
- [21] Henriques, J. P., J. J. S. de Figueiredo, L. Kirchhof, D. L. Macedo, I. Coutinho, C. B. da Silva, A. L. Melo, and M. Sousa, 2018, Experimental verification of effective anisotropic crack theories in variable crack aspect ratio medium: *Geophysical Prospecting*, **66**, 141–156.
- [22] Hudson, J. A., 1981, Wave speeds and attenuation of elastic waves in material containing cracks: *Geophysical Journal of the Royal Astronomical Society*, **64**, 133–150.
- [23] M. Kachanov, B. Shafiro, and Igor Tsukrov, 2003, *Handbook of Elasticity Solutions*: Kluwer Academic Publishers.
- [24] Marion, D., T. Mukerji, and G. Mavko, 1994, Scale effects on velocity dispersion: from ray to effective medium theories in stratified media: *Geophysics*, **59**, 1613–1619.
- [25] Nishizawa, O., and T. Yoshino, 2001, Seismic velocity anisotropy in mica-rich rocks: an inclusion model: *Geophysical Journal International*, **145**, 19–32.
- [26] Poletto, M., H. L. Junior, and A. J. Zattera, 2014, *Polystyrene : synthesis, characteristics, and applications*: Nova Science Publishers.
- [27] Rathore, J., E. Fjaer, R. Holt, and L. Renlie, 1995, P- and S-wave anisotropy of a synthetic sandstone with controlled crack geometry: *Geophysical Prospecting*, **43**, 711–728.
- [28] Santos, L. K., J. J. S. de Figueiredo, and C. B. da Silva, 2016, A study of ultrasonic physical modeling of isotropic media based on dynamic similitude: *Ultrasonics*, **70**, 227–237.
- [29] Santos, L. K., J. J. S. de Figueiredo, B. Omoboya, J. Schleicher, R. R. Stewart, and N. Dayur, 2015, On the source-frequency dependence of fracture-orientation estimates from shear-wave transmission experiments: *Journal of Applied Geophysics*, **114**, 81–100.
- [30] Santos, L. K., J. J. S. de Figueiredo, C. B. Silva, D. L. Macedo, and A. M. Leandro, 2017, A new way to construct synthetic porous fractured medium: *Journal of Petroleum Science and Eng.*, **Accepted**.

- [31] Tak, H., J. Choi, S. Jo, and S. Hwang, 2017, Stress anisotropy analysis and its effect on unconventional resource development in Montney play, Kakwa, Canada: *Journal of Applied Geophysics*, **139**, 177–187.
- [32] Thomsen, L., 1986, Weak elastic anisotropy: *Geophysics*, **51**, 1954–1966.
- [33] ———, 1995, Elastic anisotropy due to aligned cracks in porous rock1: *Geophysical Prospecting*, **43**, 805–829.
- [34] Tillotson, P., M. Chapman, A. I. Best, J. Sothcott, C. McCann, W. Shangxu, and X.-Y. Li, 2011, Observations of fluid-dependent shear-wave splitting in synthetic porous rocks with aligned penny-shaped fractures: *Geophysical Prospecting*, **59**, 111–119.
- [35] Wang, D., S. L. Qu, Q. Zhao, X. Y. Yin, and F. Zhou, 2017, Laboratory studies of ultrasonic wave response of fractures with different lengths: Anisotropy characteristics and coda analysis: *Ultrasonics*, **80**, 101–112.
- [36] Yan, F., D.-h. Han, and Q. Yao, 2015, Physical constraints on c_{13} and δ for transversely isotropic hydrocarbon source rocks: *Geophysical Prospecting*, **64**, 524–1536.
- [37] Yue, C., and X. Yue, 2017, Simulation of acoustic wave propagation in a borehole surrounded by cracked media using a finite difference method based on Hudson’s approach: *Journal of Geophysics and Engineering*, **14**, 633–640.